

Instability of forced planar liquid jets: mean field analysis and nonlinear simulation

S. Schmidt^{1,†} and K. Oberleithner¹

¹Laboratory for Flow Instability and Dynamics, Technische Universität Berlin, 10623 Berlin, Germany

(Received 7 March 2019; revised 6 September 2019; accepted 17 October 2019)

The stability of forced planar liquid jets in a still gaseous environment is explored using nonlinear simulation and spatial linear stability analysis. Harmonic modulation of the transverse component of the inlet velocity leads to an excitation of sinuous modes in the jet. Two forcing amplitudes, 1% and 5%, are investigated. While for 1% forcing, the interfacial disturbance retains a sinuous shape throughout the domain, for 5% forcing, an increasing downstream deviation from the sinuous wave shape is found. Both forcings lead to sufficient mean flow correction to render linear stability analysis on a base flow unfeasible. Hence, an analysis on the time-averaged mean flow is performed. A correction scheme is introduced, to account for the spreading of the interface position in the mean flow. Comparison of eigenfunctions and growth rates with their counterparts from the nonlinear simulation shows an excellent agreement for 1% forcing. For 5% forcing, agreement of the eigenfunctions deteriorates significantly and growth rates are falsely predicted, resulting in a breakdown of the stability model. Subsequent analysis reveals a strong interaction of the fundamental wave with the second higher harmonic wave for 5% forcing and a reversed energy flow from the coherent motion to the mean flow. These findings provide an explanation for the failure of the linear stability model for large forcing amplitudes. The study extends the applicability of mean flow stability analysis to convectively unstable planar liquid/gas jets and supports previous findings on the limits of mean flow stability, involving pronounced influence of higher harmonic modes.

Key words: absolute/convective instability, gas/liquid flows, nonlinear instability

1. Introduction

The breakup of liquid jets is relevant to a broad range of industrial applications, including ink-jet printers or fuel injection in e.g. diesel engines or gas turbines. In such cases a high-velocity liquid stream is injected into a still gaseous environment through a high pressure nozzle. The resulting two-fluid system is subjected to extrinsic and intrinsic mechanisms of destabilisation. Extrinsic factors, for instance, are given by pressure fluctuations in the supplied liquid stream or forced oscillatory movement of the jet within the nozzle. Forced destabilisation can be achieved with the use of a fluidic oscillator, to create a spatially or temporarily oscillating jet (Bobusch *et al.* 2013; Krüger *et al.* 2013; Schmidt *et al.* 2018). These effects possibly promote the development of intrinsic destabilisation mechanisms that arise through the shear of the

[†] Email address for correspondence: s.schmidt@fdx.de

adjacent parallel fluid layers, the presence of surface tension at the liquid/gas interface or unstable stratification of denser and lighter fluid.

Besides experiments or direct numerical simulation (DNS) to capture the full nonlinear dynamics of the flow, assessment of the various occurring flow instability can be made by means of linear stability analysis (LSA). The early studies of Rayleigh (1878) consider the inviscid analysis of a low-velocity cylindrical liquid jet. In this configuration disturbances in the jet radius, and thus in the capillary pressure gradient, with wavelengths exceeding the jet perimeter may grow in time and break up the jet under the influence of surface tension.

Investigations by Squire (1953), however, showed that surface tension acts stabilising if the jet is planar since there is no circumferential connection of the upper and lower interface. Instability has therefore to be rooted in the shear layer of the fluids, caused by either the momentum, density or viscosity defect (Yih 1967; Drazin & Reid 2004). With increasing jet velocity aerodynamic effects become relevant. Thus the incorporation of the surrounding fluid is necessary as investigated by Hagerty & Shea (1955) for an inviscid ambient gas and later in the studies of Lin, Lian & Creighton (1990), Li & Tankin (1991) and Li (1993) for a viscous gas. However, none of these considered a gas boundary layer, which was studied by e.g. Tammissola *et al.* (2011). For a fully viscous shear layer, approximated by a tanh-profile, Boeck & Zaleski (2005) found three competing unstable modes, attributed to the viscosity ratio (H mode), the inviscid Kelvin–Helmholtz and the viscous Tollmien–Schlichting mechanism. In the context of plane liquid jets Söderberg (2003) found up to five unstable modes, three asymmetric and two symmetric modes, using both spatial and temporal LSA. The jet velocity profile was obtained by numerical analysis and the gas velocity profile was approximated by a spatial transformation of Stokes first problem (Schlichting & Gersten 2006). Downstream amplitude growth was evaluated and compared to experimental results with good agreement. Similarly, a cylindrical jet in the first wind-induced break-up regime was analysed by Gordillo & Pérez-Saborid (2005) using a constant jet velocity. In the above works either the gas-phase or liquid-phase base flow profiles were modelled using analytical approximations of the actual velocity profile. A fully numerical base flow computation by means of DNS was used by Tammissola, Lundell & Söderberg (2012) for global stability analysis of confined planar liquid jets and wakes.

The classical approach to LSA by linearising the Navier–Stokes operator around a theoretical, steady base flow, however, neglects possible nonlinear dynamics of the underlying flow as well as any incoherent, turbulent fluctuations. A way to account for these aspects is to linearise around the time-averaged mean flow. The approach has been successfully used for e.g. the prediction of finite vortex shedding behind a cylinder at post-critical Reynolds numbers (Pier 2002; Barkley 2006) or the spatial development of a forced single-phase jet (Oberleithner, Rukes & Soria 2014*b*). Limits of the mean flow model have been revealed by Sipp & Lebedev (2007) for an open cavity flow due to significant resonance of the fundamental wave with its first harmonic. To the best of the authors knowledge the concept of mean flow stability has not been applied to the scenario of forced liquid jets so far.

In the present work a jet is forced sinusoidally at the domain inlet, resulting in the development of finite amplitude waves that grow and decay in the downstream direction, resulting in a convectively unstable flow. The aim of the investigation is twofold. First, we explore the potential of the mean field model for LSA to predict the spatial development of the excited instability waves in a forced liquid jet. Modelling using mean flow analysis has the potential of providing a simplified model to capture coherent structures of an unsteady flow without the necessity of

computing the full nonlinear representation of the flow. Second, the subsequent downstream nonlinear evolution of fundamental wave and interaction with developing higher harmonic waves are studied using direct numerical simulation of the jet. The fully nonlinear, unsteady flow representation also allows for a thorough study of the phenomenological manifestation of the nonlinear wave interaction in the flow.

The paper is structured as follows: In §2 we briefly summarise the numerical methods and present the general results of the nonlinear simulation to establish a phenomenological overview of the studied cases. In §3 the mean flow perturbation equations are derived and the methodology for two-phase flows is explained. We present the parameterisation of the mean flow and analyse general stability properties of an unforced and forced jet. A detailed comparison of the nonlinear results and the LSA is conducted in §4 where growth rates and mode shapes, derived for both methods, are presented. To conclude, in §5 shortcomings of the stability model are investigated by help of the nonlinear simulations. The developing nonlinearities in the downstream development of the excited waves are analysed and linked to the vortex dynamics of the unsteady flow.

2. Nonlinear simulation of a liquid jet

Physically, the conservation laws for flows involving two immiscible and incompressible fluids are derived with two additional assumptions over the single-phase formulation, regarding the interface, separating the two phases. First, the interface is assumed to have negligible thickness, resulting in a discontinuity of the density and viscosity field. Second, the imbalance of molecular forces along the fluid interface results in a surface tension force located at the interface. Consequently, velocity and tangential stress are continuous across the interface, while the normal stress encounters a jump, balanced by the surface tension. Numerically, the system is modelled in a unified formulation over both phases, known as the one-fluid formulation (Tryggvason, Scardovelli & Zaleski 2011), where continuity equation and momentum balance are given by

$$\frac{\partial \rho}{\partial t} + \frac{\partial \rho u_i}{\partial x_i} = 0, \tag{2.1a}$$

$$\rho \left(\frac{\partial u_i}{\partial t} + u_j \frac{\partial u_i}{\partial x_j} \right) = - \frac{\partial p}{\partial x_i} + \frac{\partial}{\partial x_j} \left[\mu \left(\frac{\partial u_i}{\partial x_j} + \frac{\partial u_j}{\partial x_i} \right) \right] + \sigma \kappa n_i \delta_S, \tag{2.1b}$$

with $u_i = (u, v)^T$ representing the components of the velocity vector ($i = 1, 2$), $x_i = (x, y)^T$ the spatial coordinates, ρ the density, μ the dynamic viscosity and p the pressure. The density and viscosity field are given as

$$\rho = \rho_g + (\rho_l - \rho_g)C, \tag{2.2a}$$

$$v = v_g + (v_l - v_g)C, \tag{2.2b}$$

where the indices g and l refer to the gaseous and liquid phase, respectively. Thus, density and viscosity vary between the phases but are constant within each phase. The volume fraction $C(x_i, t)$ is a Heaviside function, defined as the ratio of liquid volume to total volume.

The term $\sigma \kappa n_i \delta_S$ in (2.1b) accounts for surface tension forces along the interface where σ denotes the surface tension coefficient, κ is the mean interface curvature and n_i is the outward pointing normal vector. It is formulated according to the continuum surface force method (CSF) (Brackbill, Kothe & Zemach 1992). The equations

are solved using the finite volume method in the open-source toolbox BASILISK, developed by Stéphane Popinet (<http://basilisk.fr>). For a detailed description of the implemented numerical schemes, see Popinet (2003, 2009).

The interface is tracked with the volume-of-fluid (VoF) method (Hirt & Nichols 1981) using the advection of $C(x_i, t)$ as

$$\frac{\partial C}{\partial t} + \frac{\partial C u_i}{\partial x_i} = 0. \quad (2.3)$$

Computational cells where $C = 1$ are located in the liquid phase and cells with $C = 0$ are situated in the gaseous phase. Consequently, in interfacial cells $0 < C < 1$. Given the velocity field, the volume fraction field is successively advected along each dimension with a one-dimensional scheme. The local volume fraction fluxes are calculated from the local velocities and geometric reconstruction of the interface. In two dimensions the interface segment, dividing a computational cell, is reconstructed by knowledge of the value of C in the cell. Therefore, the orientation of the segment is evaluated by computing the normal vector to the segment $n_i = \partial C / \partial x_i$. The segment then is described by $n_i x_i = c$, where c is the shortest distance from the segment to the current coordinate below the segment. In practice, c can be determined by an analytic formula (Scardovelli & Zaleski 1999).

The surface tension term in (2.1b) is implemented using a balanced CSF formulation (Francois *et al.* 2006) to avoid the problem of parasitic currents (Harvie, Davidson & Rudman 2006). The method relies on an accurate computation of the interface curvature which is obtained with a height-function method, that gives second-order accurate curvature estimates (Torrey *et al.* 1985; Cummins, Francois & Kothe 2005).

For large density ratios in e.g. water/air flow, a momentum conserving scheme is used for the advection term in (2.1b) in order to avoid numerical instabilities.

The spatial discretisation is based on a uniform or non-uniform structured grid. In the latter case, a hierarchical quad-/octree structure is used to dynamically refine the grid at each time step according to a specified adaptation criterion. The dynamic grid helps to retain a high resolution in regions of large gradients while simultaneously allowing for coarse resolution away from the region of interest and therefore greatly decreases computational costs.

2.1. Problem formulation

The BASILISK solver is used to simulate the temporal and spatial evolution of a transversely forced planar liquid jet in a still ambient gas. The computational domain is square with an edge length $L = 200D$, the inlet has a width $D = 2 \times 10^{-3}$ m and is located in the centre of the left boundary. The computational domain is significantly larger than the relevant area for this study. For the remaining sections of this work, only the area $-5 < y/D < 5$, $0 < x/D < 40$ will be considered and referred to as domain. The domain is initialised with $u_i = 0$, $C = 0$. We use Dirichlet boundary conditions at the inlet and impose a sinusoidal oscillation in the transverse velocity component. The inlet conditions at Ω_1 in the centre of the left domain edge reads

$$u|_{\Omega_1} = U, \quad (2.4a)$$

$$v|_{\Omega_1} = U \times A \sin(2\pi f^* t), \quad (2.4b)$$

$$\left. \frac{\partial p}{\partial x} \right|_{\Omega_1} = 0, \quad (2.4c)$$

$$C|_{\Omega_1} = 1, \quad (2.4d)$$

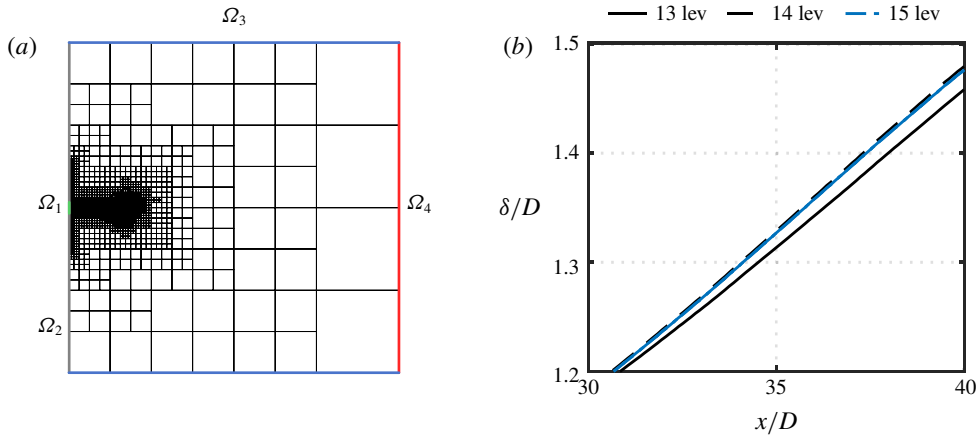


FIGURE 1. Schematic illustration of the computational domain and the adaptive grid (a) and grid sensitivity assessment using the streamwise development of the time-averaged shear layer momentum thickness δ for $A = 0.05$ (b).

where $U = 4 \text{ m s}^{-1}$ is the plug flow velocity at the inlet. The forcing frequency is $f^* = 200 \text{ Hz}$ and $A = 0.01, 0.05$. Additionally, a simulation of the unforced jet is conducted. On the remainder of the left edge (Ω_2) a no-slip boundary is imposed. The top and lower edges Ω_3 are equipped with symmetry boundaries. Along the right edge Ω_4 a standard outflow condition

$$\frac{\partial u_i}{\partial x} \Big|_{\Omega_4} = 0, \tag{2.5a}$$

$$p \Big|_{\Omega_4} = 0, \tag{2.5b}$$

$$\frac{\partial C}{\partial x} \Big|_{\Omega_4} = 0, \tag{2.5c}$$

is imposed. Further, a sponge region is employed, by enforcing a coarse mesh for $x > L/4$. Thereby, vorticity is efficiently dissipated in order to avoid backflow issues at the domain outlet. A schematic description of the computational domain is given in figure 1(a).

The fluid properties of the respective phases, corresponding to water and air, and the corresponding dimensionless quantities based on U , D and the forcing frequency f^* are given in tables 1, 2. The flow parameters and the domain extend are chosen such that the complete destabilisation cycle of the velocity field, including growth, saturation and onset of decay of the forced instability wave is captured within the area of interest. Further, the choice of flow parameters ensures that the jet remains intact throughout the domain such that no breakup of liquid structures occurs.

A dynamic quadtree-structured grid is chosen as spatial domain discretisation. To check whether a cell needs refinement, its level is reduced by one and increased again. This corresponds to down- and up-sampling of the stored scalar fields. The original field ψ is compared to the up-sampled field ψ^* to estimate the error $\epsilon = \|\psi - \psi^*\|$. The cell is refined if $\epsilon > \theta$ and coarsened if $\epsilon < 2/3\theta$ where θ is the error threshold of the specific scalar field. A more detailed description is given by van Hooft *et al.* (2018).

Name	Variable	Value	Unit
Liquid density	ρ_l	997	kg m ⁻³
Gas density	ρ_g	1.177	kg m ⁻³
Liquid viscosity	μ_l	8.90×10^{-4}	kg m ⁻¹ s ⁻¹
Gas viscosity	μ_g	1.84×10^{-5}	kg m ⁻¹ s ⁻¹
Surface tension	σ	72.5×10^{-3}	N m ⁻¹

TABLE 1. Fluid properties of the liquid and gas phase.

Name	Relation	Value
Liquid Reynolds number	$Re_l = \rho_l UD / \mu_l$	8962
Gas Reynolds number	$Re_g = \rho_g UD / \mu_g$	512
Weber number	$We = \rho_l U^2 D / \sigma$	440
Strouhal number	$St = f^* D / U$	0.1

TABLE 2. Dimensionless numbers, based on U , D and the forcing frequency f^* .

For the present work, we set $\theta = 5 \times 10^{-3}$ for both velocity components and the volume fraction. The maximum resolution is limited to 15 levels of refinement, corresponding to a minimum non-dimensional cell edge length of $\Delta x/D \approx 0.0157$. To evaluate the adequacy of the chosen adaptation criteria and mesh resolution, the time-averaged shear layer momentum thickness, defined as

$$\delta(x) = \int_0^\infty \frac{\bar{u}}{U} \left(1 - \frac{\bar{u}}{U}\right) dy, \quad (2.6)$$

where \bar{u} denotes the time-averaged streamwise velocity, is shown for 13 to 15 levels of refinement in figure 1(b). No visible improvement is seen between the latter two levels, hence the chosen parameters should be sufficient.

Simulations are run for $TU/D = 409.6$ non-dimensional time units, corresponding to 40.96 oscillation cycles. Time stepping is adaptive based, on a Courant condition

$$\Delta t \leq 0.5 \min \left\{ \frac{\Delta x}{u}, \sqrt{\frac{\rho_l \Delta x^3}{\pi \sigma}} \right\}. \quad (2.7)$$

2.2. General jet evolution

The liquid jet, injected on the left side of the domain, evolves in the streamwise direction and remains intact throughout the area of interest. The harmonic transverse forcing at the inlet introduces an initially monochromatic wave that grows in space while being convected downstream. The disturbance amplitude is clearly visible in the fluid interface, shown in figure 2, for $A = 0.01$ and $A = 0.05$. For further illustration, the envelope of the interfacial instability wave is shown for both forcing amplitudes by plotting an iso-line of the time-averaged volume fraction field \bar{C} .

For both amplitudes, the interface disturbance grows in the streamwise direction over the whole domain. For $x > 15D$ the interfacial disturbance wave starts saturating and approaches its maximum amplitude. The point where the interfacial disturbance is saturated completely is outside the investigated domain ($x/D \approx 45$). For $A = 0.05$, the

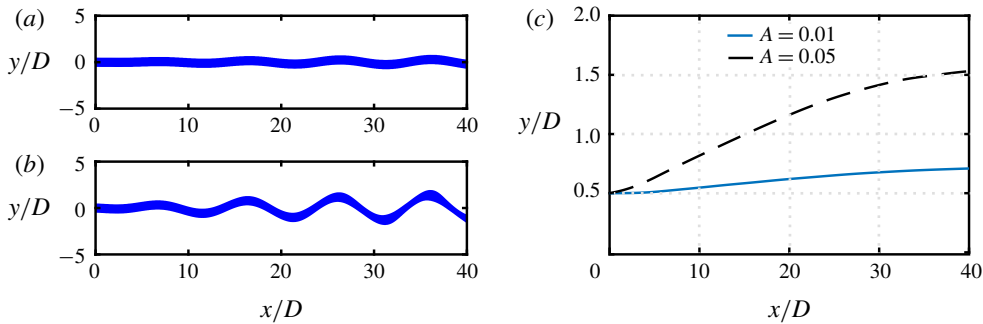


FIGURE 2. Instantaneous view of the interface via the volume fraction field C for (a) $A=0.01$, (b) $A=0.05$. The blue area corresponds to $C > 0.5$, denoting the liquid phase while the white area, $C < 0.5$, denotes the gas phase. In (c) the envelope of the interfacial instability wave is shown as an iso-line of $\bar{C}=0.01$.

influence of the harmonic forcing on the interface is much more prominent, resulting in significantly larger amplitude growth. Further, for $A=0.05$ an increasing deviation from the initial wave pattern is evident from figure 2 for $x/D > 20$. This results in a characteristic agglomeration of liquid around the wave crests as well as a shift from a sinuous wave shape to a triangular shape.

The spatio-temporal evolution of the interfacial wave and secondary structures is illustrated by the diagram of $C(x, y=0, t)$ and the instantaneous vorticity field $\Omega = \partial v/\partial x - \partial u/\partial y$ in figure 3. The contour lines of C illustrate the amplitude growth and saturation of the interfacial wave, while Ω visualises the interaction of the interface with the instability growth in the respective fluid phases. Initially, the interfacial amplitude is small and the vorticity of the liquid phase is virtually zero, which is marked as the white area in the diagram. Downstream of approximately $x/D = 10$, the amplitude growth leads to sufficient deflection of the interface to intermittently expose the growing non-zero gas-phase vorticity. In the subsequent development, the saturation of the interfacial wave is seen in the diagram as the gaps approach a constant thickness. The development of secondary structures is indicated by increasingly complex vortical patterns which manifest in the appearance of clockwise and anti-clockwise rotating vortical patterns in each gap during their downstream evolution.

For further clarification of the evolving vortical structures, the instantaneous vorticity field for both forcing amplitudes is shown in figure 4. For $A=0.01$, a single vorticity sheet evolves along each side of the interface and remains intact throughout its downstream development, indicating linear disturbance growth. Contrastingly, for $A=0.05$, the vorticity sheet in the initial shear layer is disturbed by the growing oscillation of the interface, which promotes agglomeration into discrete vortical structures from around $x/D \approx 15$. These structures develop along the interfacial wave crests when the curvature of the deflected interface becomes sufficiently large such that the vorticity sheet detaches from the interfacial curve. The formed structures travel in the wave troughs of the excited jet. While initially a single vortical structure is present, additional, secondary structures form during the downstream evolution of the jet.

Similar flow features are observable in the flow visualisation conducted by Tammissola *et al.* (2011). In their experimental work a planar liquid sheet is

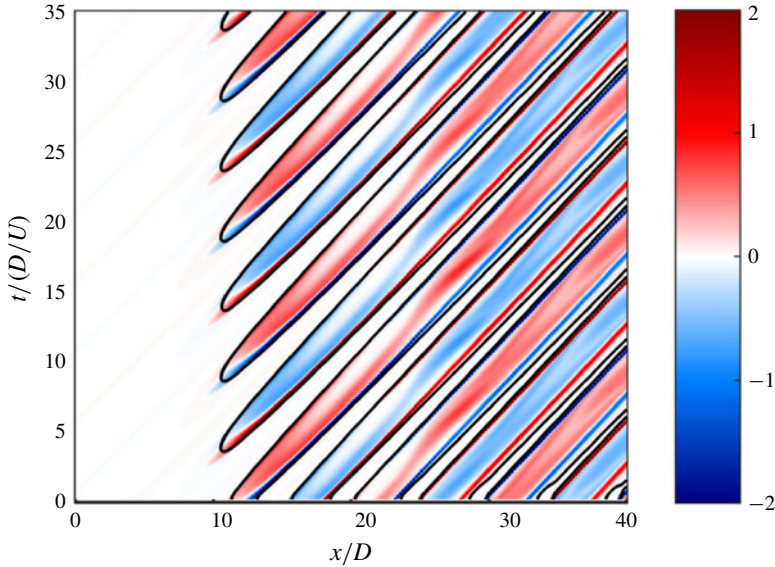


FIGURE 3. Spatio-temporal diagram of the non-dimensional centreline vorticity $\Omega/(U/D)(x, y=0, t)$ (filled contour) and the centreline volume fraction $C(x, y=0, t) = 0.5$ (black contour line) for $A = 0.05$.

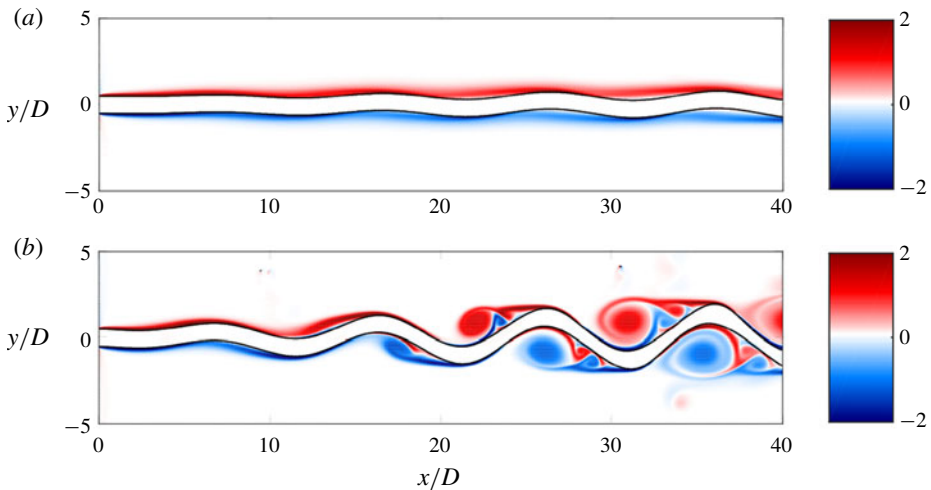


FIGURE 4. Instantaneous view of the non-dimensional vorticity field $\Omega/(U/D)$ for (a) $A = 0.01$, (b) $A = 0.05$. The interface $C = 0.5$ is shown as the black contour line.

sinusoidally forced with loudspeakers. Although their focus lies on frequency variation and the influence of gas co-flow, the sheet's response to the forcing produces comparable results to this study. In particular, for higher amplitudes, the shift from a sinusoidal to a triangular wave pattern is clearly seen. The increased interface corrugations further suggest a pronounced influence of gas-phase vorticity on the jet.

A somewhat extreme illustration of the effects of large forcing amplitudes on a liquid jet is given in Schmidt *et al.* (2018) where a liquid jet, emitted by an

industrial-type fluidic oscillator, is studied numerically and experimentally. The primary instability mechanism studied in the present case is likely to play no role at that scale, as turbulence and early onset of breakup are too pronounced for instability growth to manifest. However, it is observable that the oscillation at large amplitudes, induces significant instabilities along the liquid jet surface. These in turn, have been found to drastically facilitate jet destabilisation, leading to reduced breakup length and smaller diameters in the produced droplet spectrum.

3. Linear stability model

In this section, we establish a local linear stability model for a forced liquid jet and apply it to the configurations described in the previous section. The aim is to quantify the observed instability wave growth and decay using a simplified linear model. Therefore, we derive the linearised perturbation equations for infinitesimal disturbances of an interfacial flow. We briefly describe the implementation and validation and give notes about the parameterisation of the mean flow on which the stability analysis is conducted. Thereafter, stability properties are analysed. Special attention is given to the spatial development of the eigenfunction shapes and the corresponding growth rates.

3.1. Perturbation and mean flow equations

The derivation of the perturbation equations is based on the Navier–Stokes equations for an incompressible Newtonian fluid. In contrast to § 2, they are formulated separately for each phase as

$$\frac{\partial u_{i,l,g}}{\partial x_i} = 0, \tag{3.1a}$$

$$\frac{\partial u_{i,l,g}}{\partial t} + u_{j,l,g} \frac{\partial u_{i,l,g}}{\partial x_j} = -\frac{\partial p_{l,g}}{\partial x_i} + \frac{1}{Re_{l,g}} \frac{\partial^2 u_{i,l,g}}{\partial x_j^2}, \tag{3.1b}$$

where (3.1*b*) has been non-dimensionalised with the Reynolds number. The subscripts *l, g* denote the liquid and gaseous phase respectively. For improved readability, the phase-denoting subscripts will be dropped unless explicit distinction is necessary. For analysing the growth of intrinsic disturbances, the velocity and pressure field are decomposed into a basic state and disturbed state

$$u_i(x_i, t) = u_{b,i}(y) + \epsilon u'_i(x_i, t) \quad \text{and} \quad p(x_i, t) = p_{b,i}(y) + \epsilon p'(x_i, t), \tag{3.2a,b}$$

where $\epsilon \ll 1$ is a small amplitude. The time-independent base flow is denoted by the subscript *b*. Since a local analysis is performed, the base flow is assumed to be parallel and of the form $u_{b,i}(y) = (u_b(y), 0)^T$. The parameter ϵ will be dropped for the remainder of this work. The decomposition, equation (3.2), is substituted in (3.1). Since the base flow satisfies (3.1), all base flow terms vanish. By ignoring the nonlinear term $u'_j(\partial u'_i/\partial x_j)$ the linearised form of the perturbation equations yields

$$\frac{\partial u'_i}{\partial x_i} = 0, \tag{3.3a}$$

$$\frac{\partial u'_i}{\partial t} + u_{b,j} \frac{\partial u'_i}{\partial x_j} + u'_j \frac{\partial u_{b,i}}{\partial x_j} = -\frac{\partial p'}{\partial x_i} + \frac{1}{Re} \frac{\partial^2 u'_i}{\partial x_j^2}. \tag{3.3b}$$

The equations describe the response of the underlying steady base flow to infinitesimal disturbances. However, basing the analysis on the base flow ignores any influence of dynamic fluctuations on the time-averaged mean flow such as the nonlinear saturation of the oscillatory flow (Noack *et al.* 2003). Additionally, in case of an externally forced flow, a steady solution might not even exist. Therefore, since we are interested in the stability of the time-averaged flow, obtained from the oscillatory flow, once it has reached its limit cycle, it is appropriate to choose the triple decomposition of the flow field (Reynolds & Hussain 1972),

$$u_i(x_i, t) = \bar{u}_i(y) + \tilde{u}_i(x_i, t) + u_i''(x_i, t) \quad \text{and} \quad p(x_i, t) = \bar{p}(y) + \tilde{p}(x_i, t) + p''(x_i, t), \quad (3.4a,b)$$

where \bar{u}_i and \bar{p} are the time-averaged velocity and pressure field respectively, \tilde{u}_i, \tilde{p} the periodic parts and u_i'', p'' the fluctuating parts. Upon substitution of the ansatz into (3.1), phase averaging and time averaging, the time-averaged Navier–Stokes equations are given as

$$\frac{\partial \bar{u}_i}{\partial x_i} = 0, \quad (3.5a)$$

$$\bar{u}_j \frac{\partial \bar{u}_i}{\partial x_j} = -\frac{\partial \bar{p}}{\partial x_i} + \frac{1}{Re} \frac{\partial^2 \bar{u}_i}{\partial x_j^2} + \mathcal{F}_i, \quad (3.5b)$$

where

$$\mathcal{F}_i = -\frac{\partial}{\partial x_j} (\overline{\tilde{u}_i \tilde{u}_j}) - \frac{\partial}{\partial x_j} (\overline{u_i'' u_j''}) \quad (3.6)$$

is interpreted as nonlinear modification of the mean field by Reynolds stresses of the periodic and fluctuating field. This also implies that the mean flow is not a solution of the steady Navier–Stokes equation, as noted by Barkley (2006).

The ansatz (3.4) is inserted in (3.1), phase averaging is performed and (3.5) is subtracted, to yield the dynamic equation of the fundamental wave

$$\frac{\partial \tilde{u}_i}{\partial x_i} = 0, \quad (3.7a)$$

$$\frac{\partial \tilde{u}_i}{\partial t} + \bar{u}_j \frac{\partial \tilde{u}_i}{\partial x_j} + \tilde{u}_j \frac{\partial \bar{u}_i}{\partial x_j} = -\frac{\partial \tilde{p}}{\partial x_i} + \frac{1}{Re} \frac{\partial^2 \tilde{u}_i}{\partial x_j^2} + \mathcal{F}_i^*, \quad (3.7b)$$

where

$$\mathcal{F}_i^* = -\frac{\partial}{\partial x_j} (\tilde{u}_i \tilde{u}_j) - \frac{\partial}{\partial x_j} (\widetilde{u_i'' u_j''}). \quad (3.8)$$

For the mean flow analysis, we assume that the influence of the quadratic harmonic interactions is small, although the harmonic waves themselves might not necessarily be small. Further, we assume the fluctuating velocity is small compared to the harmonic velocity (which is demonstrated in § 5). We therefore ignore \mathcal{F}_i^* and conduct an *a posteriori* analysis of the nonlinear terms in § 5 to check the validity of this assumption.

3.2. Solution method and validation

The coherent perturbations are decomposed into Fourier modes

$$\tilde{u}_i(x_i, t) = \hat{u}_i(y)e^{i(\alpha x - \omega t)} \quad \text{and} \quad \tilde{p}(x_i, t) = \hat{p}(y)e^{i(\alpha x - \omega t)}, \quad (3.9a,b)$$

where i denotes the imaginary unit, α the streamwise wavenumber of the perturbation and ω the streamwise frequency, both of which are generally complex; \hat{u}_i and \hat{p} are the complex eigenfunctions of respective perturbations in velocity and pressure. We are interested in the spatial growth and decay of disturbances. Hence, a spatial stability analysis is pursued where ω is a known, real valued frequency and α is complex valued and unknown. The ansatz (3.9) is introduced in (3.7) to obtain the Fourier-transformed perturbation equations.

Note, that the assumption of a parallel mean flow in the present case is worth questioning. In case of a laminar unforced jet, the liquid phase might retain an approximately constant diameter and an unaltered velocity profile between two respective downstream positions. This is the case if the jet exhibits a block-like velocity profile, as in e.g. Tammisola *et al.* (2011). However, for a parabolic inflow profile (Söderberg 2003), the liquid interfaces notably contracts until it reaches a relaxed state. Additionally, the shear layer spreading within the gaseous phase invalidates the strict assumption of a parallel flow.

In case of a forced jet as in the present case, the downstream spreading of the mean flow certainly violates the parallel flow assumption for both phases. Nevertheless, local analysis has shown remarkable robustness in predicting stability properties for a variety of non-parallel flows (see e.g. Cohen & Wynanski 1987; Pier 2002; Oberleithner, Paschereit & Wynanski 2014a; Terhaar, Oberleithner & Paschereit 2015; Emerson, Lieuwen & Juniper 2016). Alternatively, axial spreading can be accounted for by using a correction scheme for weakly non-parallel flows by introducing a slowly varying axial scale (Crighton & Gaster 1976; Oberleithner *et al.* 2014b) or within the framework of parabolised stability equations (Herbert 1997; Cheung & Zaki 2010). Yet, another approach is to compute the optimal response to a forcing from the resolvent norm around the mean flow, taking into account the non-normality of the linearised operator (Beneddine *et al.* 2016). However, for the present work, the focus lies on the applicability of a simple linear model to capture the overall phenomena of the underlying nonlinear flow. A detailed representation is already available through the nonlinear simulation results. Therefore, we stick to the parallel flow assumption.

As noted above, for the analysis of immiscible interfacial flows, the perturbation equations are formulated separately for each phase (see e.g. Söderberg 2003; Gordillo & Pérez-Saborid 2005). By imposing symmetry conditions along the jet centreline, it is sufficient to only consider the top half of the jet. At the interface position, coupling conditions are formulated to satisfy (3.7) across the interface. Formally the interface position is of the form $y = h(x, t)$ and is assumed to be decomposed and perturbed similarly to (3.4) (where the fluctuations are neglected) and (3.9) so that

$$h(x, t) = \bar{h}(x) + \tilde{h}(x, t) \quad \text{and} \quad \tilde{h}(x, t) = \hat{h}(x)e^{i(\alpha x - \omega t)}. \quad (3.10a,b)$$

For an unforced jet, the mean interface position is assumed to be approximately equal to the unperturbed interface position of the steady base flow, which is taken to be constant in x . Hence, \bar{h} is constant. In the time-averaged flow of the forced state it is not. Following the triple decomposition, \bar{h} should be obtained by time

averaging the instantaneous interface positions at each x . However, this approach yields unsatisfactory results as seen in §4. Therefore, an alternative modelling approach is given in §3.3 which does not follow the triple decomposition.

For the derivation of the coupling conditions, a constant \bar{h} is assumed. Formally, these conditions are valid at the perturbed interface $h(x, t)$. However, by means of a Taylor expansion of $h(x, t)$ around $y = \bar{h}$ and by neglecting terms of second order or higher, a linear approximation at the unperturbed interface is obtained. In the following, the approximated conditions at the unperturbed interface are presented. For satisfying the continuity of the velocity across the interface, it holds that

$$\left[\tilde{u} + \bar{u} + \tilde{h} \frac{d\bar{u}}{dy} \right]_{y=\bar{h},l} - \left[\tilde{u} + \bar{u} + \tilde{h} \frac{d\bar{u}}{dy} \right]_{y=\bar{h},g} = 0, \tag{3.11a}$$

$$\left[\tilde{v} \right]_{y=\bar{h},g} - \left[\tilde{v} \right]_{y=\bar{h},l} = 0, \tag{3.11b}$$

where quantities inside $\left[\cdot \right]_{y=\bar{h},l,g}$ belong to the liquid or gas phase respectively. Further, the continuity of shear stress requires

$$\left[\frac{\partial \tilde{v}}{\partial x} + \frac{\partial \tilde{u}}{\partial y} + \tilde{h} \frac{d^2 \bar{u}}{dy^2} \right]_{y=\bar{h},l} - m \left[\frac{\partial \tilde{v}}{\partial x} + \frac{\partial \tilde{u}}{\partial y} + \tilde{h} \frac{d^2 \bar{u}}{dy^2} \right]_{y=\bar{h},g} = 0, \tag{3.12}$$

and the continuity of normal stress yields

$$\left[\tilde{p} - \frac{2}{Re_l} \frac{\partial \tilde{v}}{\partial y} \right]_{y=\bar{h},l} - \left[r\tilde{p} - \frac{2m}{Re_l} \frac{\partial \tilde{v}}{\partial y} \right]_{y=\bar{h},g} + \frac{1}{We} \frac{\partial^2 \tilde{h}}{\partial x^2} = 0, \tag{3.13}$$

where $m = \mu_g/\mu_l$ is the ratio of the dynamic viscosities of the two fluids and $r = \rho_g/\rho_l$ is the density ratio. A detailed derivation of the stress conditions is given in appendix A. The kinematic condition for the interface is

$$\left[\frac{\partial \tilde{h}}{\partial t} + \bar{u} \frac{\partial \tilde{h}}{\partial x} = \tilde{v} \right]_{y=\bar{h},l,g}. \tag{3.14}$$

Note that it is possible to formulate the kinematic condition for the gas-phase velocity at the interface as well as for the liquid-phase velocity. The coupling conditions are complemented by boundary conditions to close the system.

Only asymmetric waves are considered in the stability analysis, since in the nonlinear simulation, the jet is forced sinusoidally in the v -component of the velocity to excite asymmetric modes. From the analysis of the simulation it is evident that the dominant mode at the forcing frequency remains asymmetric throughout the downstream development of the jet and the aim of the work is to investigate the potential of the mean flow stability model to predict the growth and saturation of this forced wave. Therefore, a symmetry condition

$$\left[\tilde{u} = 0, \frac{\partial \tilde{v}}{\partial y} = 0, \tilde{p} = 0 \right]_{y=0,l} \text{ for asymmetric modes} \tag{3.15}$$

is imposed, as well as a no-slip condition

$$\left[\frac{\partial \tilde{u}}{\partial y} = 0, \tilde{v} = 0, \frac{\partial \tilde{p}}{\partial y} = 0 \right]_{y \rightarrow \infty, g}. \tag{3.16}$$

	Interface mode	Shear mode
Present	1.003907431 + 0.001791888361 <i>i</i>	0.2578942009 + 0.0008778900946 <i>i</i>
Dongarra <i>et al.</i> (1996)	1.003907431 + 0.001791888368 <i>i</i>	0.2578942002 + 0.0008778915187 <i>i</i>

TABLE 3. Validation of two-layer Poiseuille flow using temporal analysis ($\alpha = 1$). The corresponding unstable eigenvalues $c \equiv \omega/\alpha$ are displayed.

The closed system (equations (3.7), (3.11)–(3.16)) with the ansatz (3.9), (3.10) is solved using a Chebyshev spectral collocation method. The grid of the liquid phase extends over $0 < y \leq \bar{h}(x)$ where $\bar{h}(x=0) = 0.5$. The grid of the gas phase extends from $\bar{h}(x) < y \leq 4D$. Each grid is discretised using $N = 110$ collocation points, resulting in $2 \times N \times 3 = 1980$ degrees of freedom. Convergence is demonstrated in appendix B. The resulting quadratic eigenvalue problem is of the form

$$(\alpha^2 \mathbf{A}_2 + \alpha \mathbf{A}_1 + \mathbf{B})\mathbf{q} = \mathbf{0}. \tag{3.17}$$

The matrices \mathbf{A}_2 , \mathbf{A}_1 and \mathbf{B} contain the mean flow profiles $\bar{u}_{l,g}$, and $\mathbf{q} = (\hat{u}_l, \hat{v}_l, \hat{p}_l, \hat{u}_g, \hat{v}_g, \hat{p}_g, \hat{h})^T$. Using the companion linearisation, equation (3.17) is reduced to a linear problem

$$\left[\begin{pmatrix} \mathbf{B} & \mathbf{0} \\ \mathbf{0} & \mathbf{I} \end{pmatrix} + \alpha \begin{pmatrix} \mathbf{A}_1 & \mathbf{A}_2 \\ -\mathbf{I} & \mathbf{0} \end{pmatrix} \right] \begin{pmatrix} \mathbf{q} \\ \alpha \mathbf{q} \end{pmatrix} = \mathbf{0}, \tag{3.18}$$

where \mathbf{I} is the identity matrix. The linear system, equation (3.18), is consecutively solved at each streamwise position using the *QZ* algorithm in MATLAB’s *eig* function, which simultaneously delivers all eigenvalues, to obtain the spatial evolution of α and the corresponding eigenfunctions. The additional eigenvalues and eigenvectors, introduced by the companion linearisation, are discarded. To validate the code, the temporal stability results of the two-layer Poiseuille flow by Dongarra, Straughan & Walker (1996) are reproduced. The resulting unstable eigenvalues are listed in table 3 and the flow conditions are restated in appendix C. As their results exclude the influence of surface tension, the results of Tammisola *et al.* (2011) (figure 16a) in their work) are qualitatively reproduced as well.

3.3. Mean flow configuration and parameterisation

The *u*-component of the mean flow velocity field is obtained by averaging 2^{11} consecutive snapshots of the fully developed flow of the nonlinear simulation in § 2 at time increments $\Delta t U/D = 0.15$ and within an area $-5 < y/D < 5$, $0 < x/D < 40$. These are mapped on an equidistant Cartesian grid with a resolution of 800×200 px where $1 \text{ px} = 1 \times 10^{-4} \text{ m}$. The mean flow field should be symmetric with respect to the jet centreline. Therefore, remaining minor asymmetries in the time-averaged flow are eliminated by taking the symmetric part

$$\bar{u}_{sym} = \frac{1}{2}(\bar{u}(y) + \bar{u}(-y)). \tag{3.19}$$

The symmetric, time-averaged mean flow is shown in figure 6.

In Gordillo & Pérez-Saborid (2005) and Tammisola *et al.* (2011) analytic base flows were used and a constant velocity profile of the liquid phase was assumed. The gas

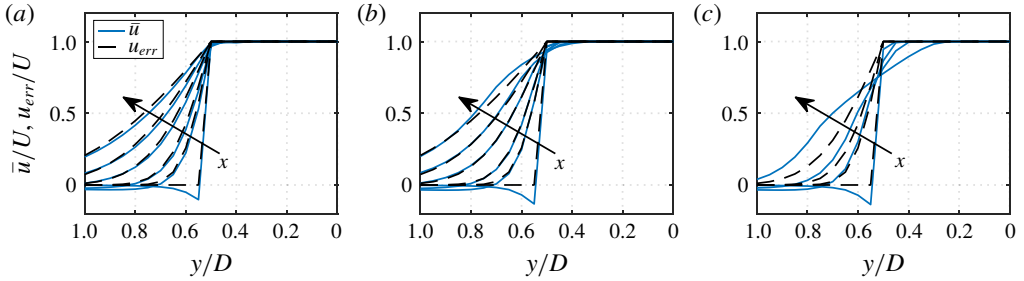


FIGURE 5. Comparison of the mean flow profiles and an error-function profile (as in Tammisola *et al.* (2011)) for the unforced flow (a), and forced flow with (b) $A = 0.01$, (c) $A = 0.05$. Plot positions are $x/D = 0.01, 1, 2, 5, 10, 20$. For $A = 0.05$, positions $x/D = 10, 20$ are omitted due to very large deviations from the error-function profile.

boundary layer was approximated using an error-function profile. A comparison of the mean flow profiles with these analytic profiles is given in figure 5. It is seen that for the unforced flow, the error-function profile slightly over-estimates the developing shear layer, although differences are minor. More prominent deviations are observed along the interface, since the assumption of a constant liquid velocity does not hold for the nonlinear simulation. Further, the zero Dirichlet condition for the gas velocity causes a reversed flow in the gas phase close to the inlet, which possibly influences the development of the initial boundary layer and could have an effect on the growth rate of the instability wave. For the forced flow, the mean flow profile quickly deviates from the error-function profile, as the oscillation significantly thickens the mean flow shear layer, especially for $A = 0.05$. In conclusion, the analytic profile might be a sufficient approximation for an unforced jet but not for a forced jet.

The necessity of modelling the position of the mean interface in the mean flow, noted in the previous section, is addressed here. Within the parallel flow framework, the interface between the liquid and gaseous phase is located at a fixed position $y = h_b$ which is determined by the solution of the underlying steady base flow. For instance, in Tammisola *et al.* (2011) and Gordillo & Pérez-Saborid (2005) the interface position remained constant in downstream direction. In Söderberg (2003) a numerical base flow for the liquid phase was computed with varying interface positions in downstream direction.

For this study a simple model is constructed, that requires the mass of the liquid phase at $x/D = 0$ to be conserved for all streamwise positions in the mean flow. The initial mass is determined by the initial interface position $\bar{h}(x = 0) = 0.5$. Then, the time-averaged density field $\bar{\rho}$ is integrated at each x , from $0 < y < \bar{h}(x)$. The upper integration bound $\bar{h}(x)$, defining the interface within the mean flow, is chosen such that

$$\int_0^{0.5} \frac{\bar{\rho}(x = 0, y)}{\rho_l D} dy = \int_0^{\bar{h}(x)} \frac{\bar{\rho}(x, y)}{\rho_l D} dy. \quad (3.20)$$

An illustration of this procedure is shown in figure 7 along with the resulting interface curve within the mean flow. As is seen, the model moves the interface reasonably into the mean flow shear layer.

When using a true stationary solution, the interface position can simply be defined by the volume fraction $C = 0.5$, as in the VoF method. However, this assumption does not hold in the time-averaged flow (for the time-averaged volume fraction

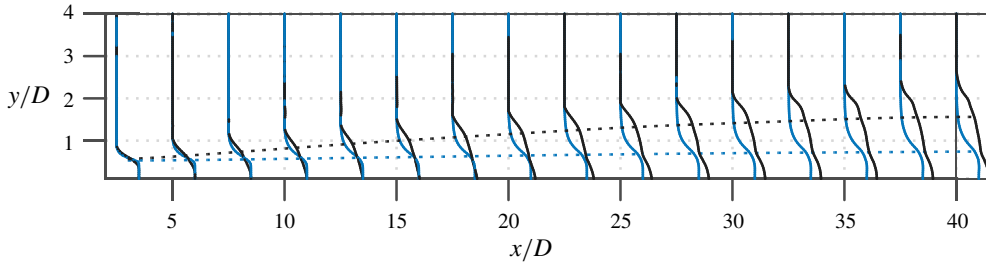


FIGURE 6. Mean flow profiles of the jet forced at $A = 0.01$ (blue); $A = 0.05$ (black). The spreading of the mean interface position, derived from figure 7, is shown as a dashed line.

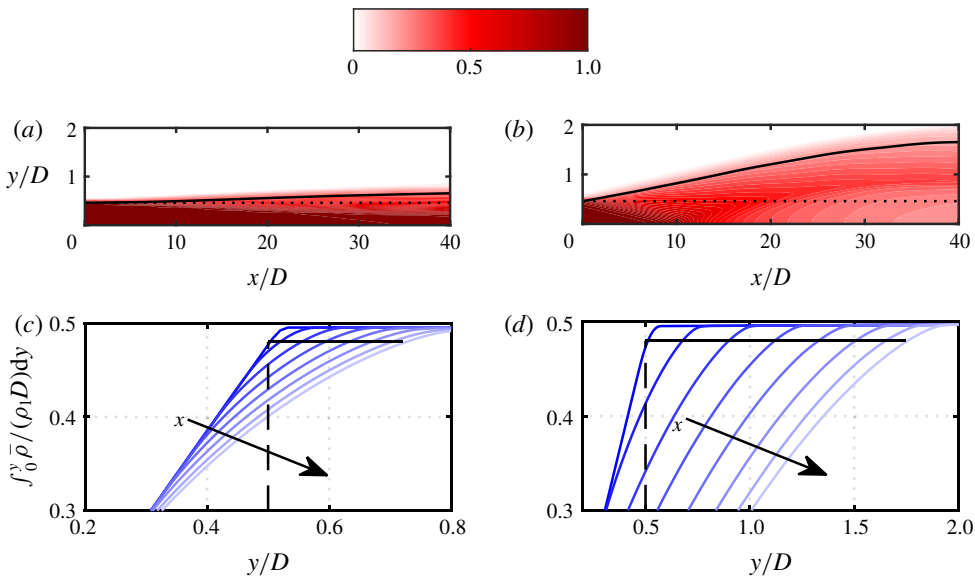


FIGURE 7. Illustration of the mean interface spreading. The top row shows a contour plot of the mean volume fraction field $\bar{\rho}/\rho_l$ of the nonlinear simulation and the interpolated interface position for the linear stability model as black line, for (a) $A = 0.01$; (b) $A = 0.05$. The black dotted line represents the presumed, fixed interface position of the unforced flow. Red areas correspond to regions of small interface amplitudes while lighter shades indicate areas of increased amplitudes. The second row shows the cumulative integral of $\bar{\rho}/\rho_l D$ along y for several streamwise positions, for (c) $A = 0.01$; (d) $A = 0.05$. The interface at $x = 0$ (vertical line) determines the initial mass of the liquid. The interface is constructed such that the liquid mass is conserved (horizontal line).

$\bar{C} \approx \bar{\rho}/\rho_l$) which is seen in figure 7: Using $\bar{C} = 0.5$ the interface would move towards the centreline of the jet. A consistent approach to obtaining the interface position according to the triple decomposition would be to take the time-averaged position. However, for a transverse sinusoidal forcing, the growing interface disturbance should approximate a growing sine wave on each side of the plane jet/sheet. As the jet oscillates symmetrically around its (theoretical) centreline, the time-averaged position of the interface would be $\bar{h}(x) = \pm 0.5$ for all streamwise positions, which corresponds to the position of the unperturbed flow. Another approach to obtain the interface

position in the mean flow that might seem plausible at first sight, is to derive the location with the highest probability of interface residence at each streamwise position, i.e. a probability density. However, for a sine wave this would yield an interface position at either of the extrema of the sine wave. This does not seem plausible, since it traverses the interface almost out of the mean flow shear layer. The effect of the interface correction is further assessed in the following sections.

3.4. General stability properties of the jet

For the stability analysis, three different cases will be of interest. The first case is based on the mean flow of the unforced jet. As within the current numerical framework, natural disturbances of the unforced jet remain very small (at least in the considered domain), it closely corresponds to an equilibrium or base flow solution, i.e. the interface remains at the initial, unperturbed position within the sampling accuracy ($\bar{h}(x) = 0.5$), as has been carefully checked. We denote this case as the base flow model. The second case is based on the mean flow of the forced jet but ignores the interface displacement in the mean flow, such that $\bar{h}(x) = 0.5$ (equivalent to a triple decomposition of the interface). This case is denoted as the fixed interface model. The third case is similar to the second one but includes the proposed interface correction model to account for the interface displacement. This case is denoted as the varying interface model.

To obtain a general overview on the stability properties of the present jet configuration, in figures 8(a) and 8(b) the streamwise distribution of spatial growth rates is derived for the base flow model for a broad range of frequencies. There are two unstable modes found which together render the jet convectively unstable for all applied frequencies within the displayed domain.

In detail, mode I is unstable for all shown frequencies and shows an increasing maximum growth rate as the frequency increases up to $fD/U = 0.27$. Characteristic for this mode are the almost vertical contour lines within the initial region of the jet, that make the upstream stability behaviour of the jet virtually similar for a range of applied frequencies of approximately $0.1 < fD/U < 0.3$. The upstream appearance of the mode is qualitatively reminiscent of the sinuous mode of type I found in Söderberg (2003).

For frequencies $fD/U < 0.27$ mode II is unstable as well in the upstream region of the jet. However, prolonged downstream influence of this mode is only observed for $fD/U < 0.1$, where the point of neutral stability moves beyond $x/D = 10$. Contrasting with mode I, the contour lines follow a more horizontal trend, especially in the lower frequencies. Additionally, the mode shows significantly smaller growth rates within the initial jet region, compared to mode I. The low-frequency region of this mode partially resembles the sinuous mode of type II found in Söderberg (2003). For better comparison the stability maps are re-plotted in appendix D, using similar scaling as in Söderberg (2003). However, in contrast to his findings, no third unstable physical eigenvalue is found for the present configuration.

There is however one additional marginally stable eigenvalue found which might correspond to the third mode found in Söderberg (2003), but since it is not unstable we shall not investigate it further in this work. Also mode II is either stable or exhibits weaker growth for the forcing frequencies applied in this work and thus will be excluded from further investigations as well.

The stability map of mode I is also derived for the fixed and varying interface model with $A = 0.01$ at $St = 0.1$ in figure 8(d). As can be seen, the mean flow for the

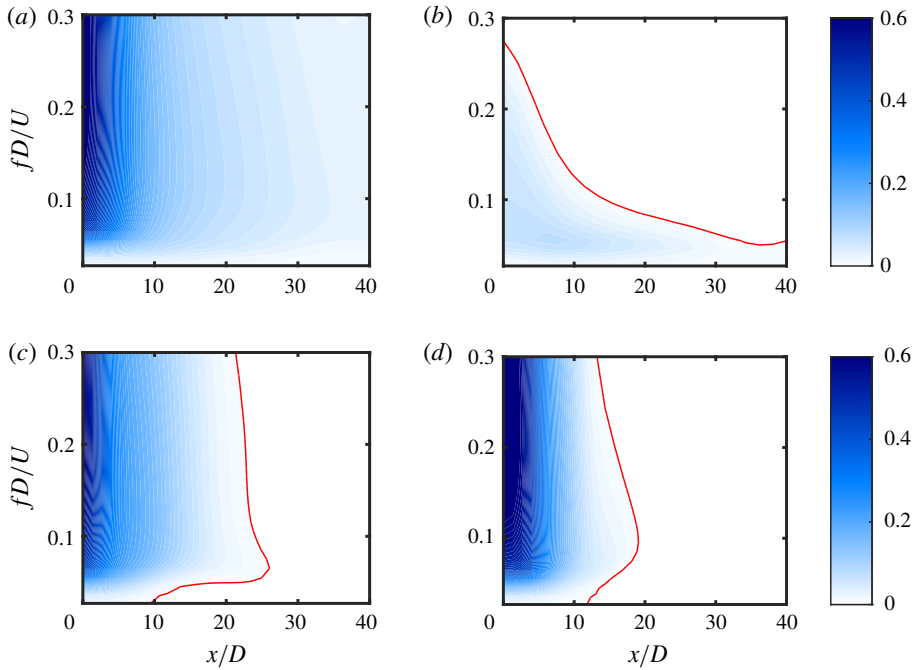


FIGURE 8. Stability map for the base flow model: mode I (a), mode II (b), fixed interface model (mode I) at $A = 0.01$ (c), varying interface model (d). Shown is the spatial growth rate $-\alpha_i D$ and the curve indicating neutral stability, i.e. $\alpha_i D = 0$, in red.

fixed interface model significantly alters the stability map. Using the forced flow, the threshold for neutral stability moves into the domain for all frequencies and is located between $x/D = 20$ and $x/D = 30$ for $fD/U > 0.05$. For lower frequencies the neutral point reaches approximately $x/D = 10$. When the displacement of the mean interface position is taken into account (varying interface model), the neutral stability curve shifts even further upstream for most frequencies and renders all positions downstream $x/D = 20$ stable. This indicates that the spreading of the mean interface has indeed an impact on the stability properties of the jet even at small forcing amplitudes and as shown below is even necessary to correctly recover the point of neutral stability of the excited instability wave. The maps derived for the fixed and varying interface model are obtained using the time-averaged flow at $St = 0.1$. Therefore, the growth rates shown in figures 8(c) and 8(d) correspond to modes existing on this specific mean flow. For deriving maps where the displayed growth rates correspond to the most unstable eigenmode at the forcing frequency, a separate mean flow with a forcing at the respective frequency would have to be used for each eigenmode.

The origin of the unstable mode can be inspected by analysing its energy budget, as carried out by Boomkamp & Miesen (1996) and Otto (2012). Therefore, an energy balance over both fluid phases is derived as

$$MFL_l + MFL_g = REY_l + REY_g + TAN + NOR + DIS_l + DIS_g, \quad (3.21)$$

where MFL corresponds to the streamwise mean energy flux. The flux is balanced by a production term accounting for energy transfer from the mean flow to the perturbation through Reynolds stresses REY. The energy transfer to the velocity

Case	St	A	REY_g	REY_l	TAN	NOR	DIS_g	DIS_l
Fixed interface model	0.1	0.01	0.0012	0.0180	0.9903	0.0074	-1.4354×10^{-4}	-0.0168
Varying interface model	0.1	0.01	0.0014	0.0580	0.9424	0.0107	-1.3422×10^{-4}	-0.0124
Fixed interface model	0.1	0.05	0.0005	0.1066	0.8844	0.0262	-2.9122×10^{-4}	-0.0175
Varying interface model	0.1	0.05	0.0013	0.5085	0.4395	0.0557	-2.6337×10^{-4}	-0.0047

TABLE 4. Energy budget of mode I of the linear stability model at $x/D = 10$.

perturbations along the interface is accounted for by TAN and NOR, representing the work of tangential and normal stress. The perturbation energy dissipation is given by DIS. It is always negative by definition while the sign of the other quantities might change depending of the flow configuration. Every quantity is normalised by the sum of all quantities. The complete expressions for the respective terms are given in appendix E. The contributions of the respective terms, calculated exemplarily at $x/D = 10$, are given table 4.

For $A = 0.01$ the energy budget is dominated by the contribution of tangential stresses, caused by the viscosity jump across the interface. Additionally, the energy transfer from the mean flow to the perturbed flow through Reynolds stresses within the liquid phase as well as the contribution of normal stresses from the pressure jump have some influence, although they are significantly weaker than the tangential stresses. Energy dissipation almost exclusively takes place in the liquid phase. Overall the gaseous phase has negligible contribution to the perturbation energy budget. For increased forcing the influence of TAN and REY_g decreases while for REY_l and NOR it increases.

The interface correction is seen to increase the influence of the REY_l and lower the influence of TAN which is to be expected since the correction shifts the interface position outwards into the mean flow shear layer where the mean flow gradient is larger than in proximity to the jet centreline and so are the Reynolds stresses.

When comparing the contributions at the respective amplitudes it is seen that the contribution of REY_g decreases for increasing forcing amplitude which seems counter-intuitive. However, due to the increased mean flow spreading for larger forcing amplitudes, the transverse gradient of the mean flow velocity in the gas phase, as seen in figure 6, reduces which provides an explanation for the lower values of REY_g . In contrast, the gradient within the liquid part of the mean flow shows a slight increase which is in line with the increase of REY_l for larger forcing amplitudes.

4. Comparison of nonlinear simulation and linear stability model

The findings of the previous section have shown plausible results for $A = 0.01$ when the streamwise spreading of the mean interface position is accounted for. In the following, the eigenfunctions and corresponding growth rates of the stability analysis are compared to their equivalents from the nonlinear simulation (DNS). Therefore, a decomposition of the coherent flow field of the DNS into a Fourier series yields the complex Fourier coefficients

$$\hat{u}_{i,n}(x_i) = \frac{1}{2\pi T} \sum_{n \neq 0} \tilde{u}_i e^{-i2\pi nft}. \quad (4.1)$$

To obtain the coherent velocity \tilde{u}_i , formally, \bar{u}_i is subtracted from the phase-averaged velocity field to exclude any incoherent fluctuations. However, as demonstrated in § 5,

the incoherent motion is negligibly small compared to the coherent motion. Therefore, $\tilde{u}_i \approx u_i - \bar{u}_i$ has proven to be an adequate choice.

We investigate the potential of the linear model for both forcings $A = 0.01$ and $A = 0.05$. For the sake of completeness and to underline the benefits of the mean flow model, the main results of this section are reproduced for the base flow model in appendix F.

4.1. Streamwise and cross-wise eigenfunctions

The eigenfunctions \hat{u} and \hat{v} of the linear stability analysis and the fundamental wave packet ($n = 1$) of the DNS, derived from (4.1), are shown in figure 9. The region of linear growth is followed by the nonlinear saturation and decay of the amplitude.

For $A = 0.01$ and the fixed interface model, an overall very good agreement is found for \hat{v} . Particularly in the gaseous part of the shear layer, there is an excellent correspondence of the eigenfunctions throughout the domain. Along the liquid jet centreline, amplitude prediction is very good as well up to approximately $x/D = 20$. However, beyond that point there are some visible discrepancies around the interface where the steep gradient of the amplitude is not followed as rigorously by the linear model. For $x/D > 30$ the agreement between simulation and linear stability model deteriorates further within the liquid part of the shear layer. The under-prediction for $x/D < 5$ within the liquid phase is possibly attributed to the influence of the inlet wall in the simulation, which should approximately resemble the nozzle in the experiments of Orszag & Crow (1970) and Oberleithner *et al.* (2014b). They argue that discrepancies in this area are likely caused by an interaction of the instability wave with the nozzle that is not covered by the linear model. For \hat{u} similar agreement is found. The discrepancies along the interface are seen here as well and visualised as a slight lateral shift of the amplitude maximum.

For the varying interface model the eigenfunctions of linear stability analysis and their equivalents of the DNS become virtually indistinguishable throughout the domain (apart from the near-nozzle region that remains unaffected by the correction). This shows that accounting for the displacement interface in the spreading mean flow is indeed necessary to obtain a correct representation of the eigenfunctions. In conjunction with the findings in table 4, neglecting the interface spreading leads to a under-representation of Reynolds stresses in the mean flow stability model and an insufficient representation of the perturbation shear layer.

For \hat{u} a similar trend is found. With the fixed interface model, increasing discrepancies along the interface are seen here as well for $x/D > 15$ and manifest in the absence of a lateral shift of the amplitude maximum as well as the formation of an erroneous double spike in the amplitude. For the varying interface model, the outward spreading of the amplitude is followed by the linear model.

For $A = 0.05$, the overall agreement is significantly less accurate. Nevertheless for $x/D < 20$, the \hat{v} -component shows very good agreement despite the significant transverse spreading of the shear layer (varying interface model). With the fixed interface model this trend is not followed, resulting in visible deviations already at $x/D = 7.5$. However, beyond $x/D = 20$ both methods fail to correctly represent the wave packet amplitude of the nonlinear flow. The portrayal of \hat{u} shows the same trend, though the qualitative differences are somewhat more pronounced.

4.2. Growth rates and phase velocity

In the linear model, growth rates of the instability wave are readily given through the imaginary part of the eigenvalue α_i , introduced in (3.9). Deriving a correspondent

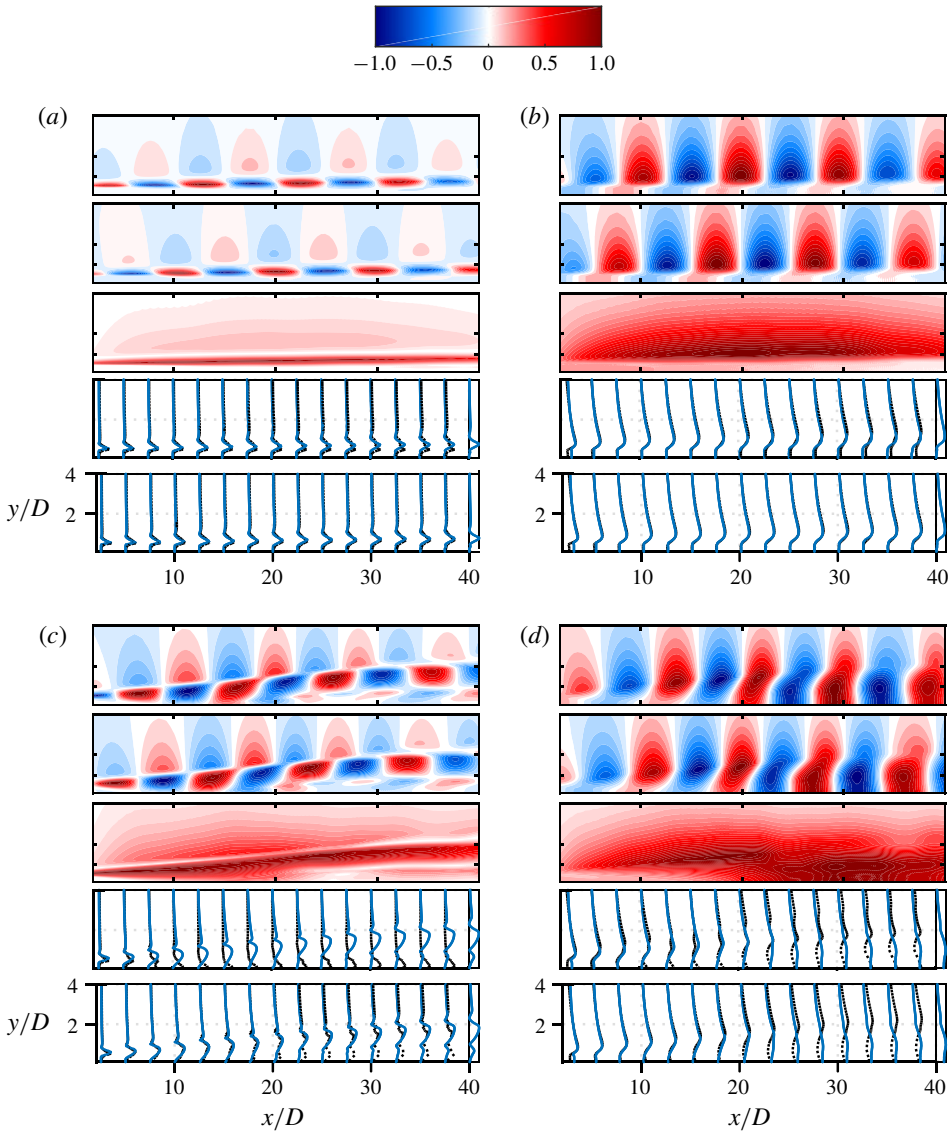


FIGURE 9. Illustration of the fundamental wave packet ($n = 1$), obtained from the DNS and comparison of the computed amplitude functions from the linear stability model and the DNS for (a) $A = 0.01$, \hat{u} ; (b) $A = 0.01$, \hat{v} ; (c) $A = 0.05$, \hat{u} ; (d) $A = 0.05$, \hat{v} . Panels show, from top to bottom, the real part, imaginary part, the absolute value and corresponding amplitudes (for the fixed and varying interface model) normalised by their maximum value. Blue lines show the DNS while black lines show the LSA.

measure for the amplitude growth from the DNS introduces an ambiguity to the analysis. For the present work, the most suitable measure was found to be based on the energy norm of the two-phase velocity field. The amplitude is computed as

$$\tilde{A}_n(x; \hat{\rho}_n; \hat{u}_n; \hat{v}_n) = \frac{\sqrt{2}}{UD/2} \left(\int_0^\infty |\hat{\rho}_n| [|\hat{u}_n|^2 + |\hat{v}_n|^2] dy \right)^{1/2}, \quad (4.2)$$

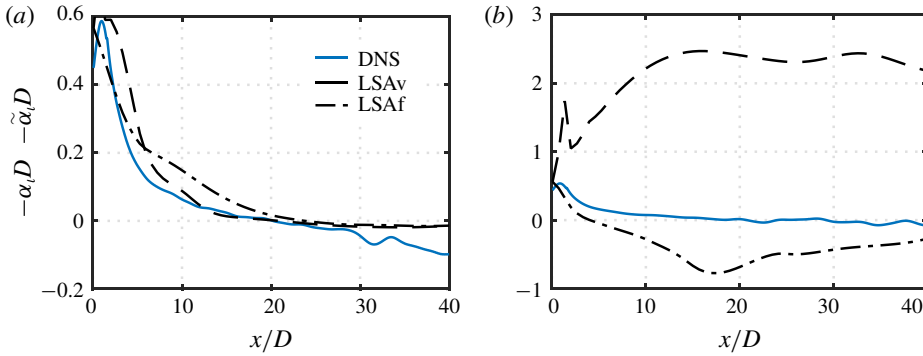


FIGURE 10. Comparison of the computed growth rates $-\alpha_t D$ from the linear stability model and $-\tilde{\alpha}_t D$ from the DNS for (a) $A=0.01$, (b) $A=0.05$. DNS denotes the nonlinear simulation, LSAv and LSAf the varying and fixed interface model.

where $\hat{\rho}_n, \hat{u}_n, \hat{v}_n$ are obtained from (4.1). This corresponds to the amplitude of the velocity fluctuation of the respective harmonics, integrated across the shear layer of the jet (Delbende, Chomaz & Huerre 1998; Oberleithner *et al.* 2014b). Other plausible energy norms include a separate formulation for the velocity of the respective fluid phases or a formulation for the density field only. A separate measure of the velocity of each fluid phase did not reveal any significant differences in the evolution of the growth rates as compared to the chosen method. However, when using a formulation over the density field, a slower decay of the instability wave is observed (not shown). The streamwise growth rate then is defined as

$$-\tilde{\alpha}_t(x) = \frac{d(\ln \tilde{A}_t)}{dx}. \tag{4.3}$$

The predicted growth rates of both models are given in figure 10. For $A = 0.01$, very good agreement is reached between the DNS and the linear stability model. For the fixed interface model, the growth rates in the initial region up to $x/D = 5$ are very well recovered. Thereafter, the predicted growth rate decreases slower than in the DNS leading to a slightly delayed saturation and zero crossing of the growth rate of the linear model. Further downstream, the stable wave decays slightly slower than predicted by the DNS. Using the varying interface model, the initial growth rate is slightly over-predicted. However, for $10 < x/D < 30$ an excellent agreement is found and the neutral point is (if slightly under-predicted) recovered better than for the fixed interface model. In comparison, the growth rates obtained from the base flow model (appendix F) do not predict the neutral point to be within the considered domain at all. Therefore, the mean flow model generally seems to yield more accurate results than the base flow model.

For $A = 0.05$ in figure 10(b), the agreement of the predicted growth rates is poor throughout the domain, which is to be expected from the substantial deviations of the eigenfunctions shown above. The fixed interface model predicts the instability wave to decay much faster than in the DNS, leading to a significant under-prediction of the neutral point. For the varying interface model, the growth rate prediction of the linear model is even worse and predicts an increasing destabilisation of the instability wave such that no saturation is predicted at all.

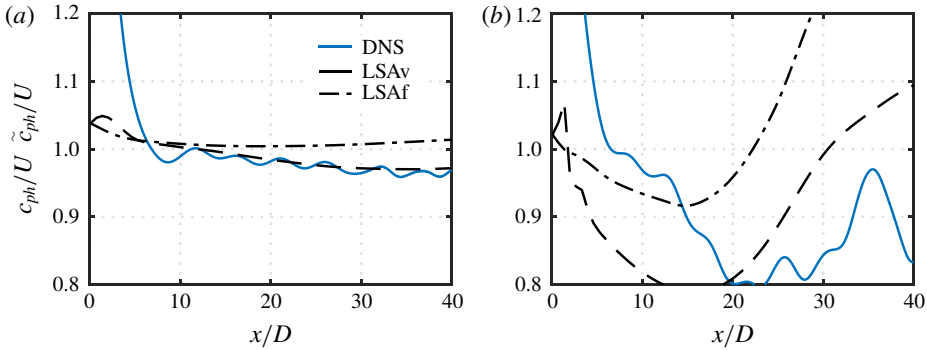


FIGURE 11. Comparison of the computed phase velocities c_{ph}/U from the linear stability model and \tilde{c}_{ph}/U from the DNS for (a) $A=0.01$, (b) $A=0.05$. DNS denotes the nonlinear simulation, LSAv and LSAf the varying and fixed interface model.

To compare the real part of the eigenvalue, α_ρ , to the wavelength of the forced instability, observed in the DNS, the phase velocity is derived as $c_{ph} = \omega/\alpha_\rho$. The corresponding phase velocity $\tilde{c}_{ph}(x)$ from the DNS is obtained by the relation $\alpha_\rho = (\partial\phi/\partial x)$, where we define an integral measure for the phase angle of the fundamental wave as $\phi(x) = \int_0^\infty \arg(\hat{v}_1(x, y)) dy$.

The comparison of the LSA and the DNS is shown in figure 11. For $A=0.01$ very good agreement away from the near-nozzle region $x/D > 10$ is found for the varying interface model. For the fixed interface model, slightly increasing deviation is observed downstream around $x/D = 15$. For $A = 0.05$, agreement deteriorates, which is to be expected in light of the poor reproduction of the growth rates at this forcing amplitude. However, by taking the interface displacement into account the trend seen in the DNS is partially recovered and the overall quantitative discrepancies are reduced.

4.3. Relation to previous studies on the stability of forced liquid jets

From the body of literature available on the linear stability of liquid jets, the works of Söderberg (2003) and Tammissola *et al.* (2011) were found to bear closest resemblance to the present study and a brief comparison shall be conducted here.

Although the forcing frequencies in Tammissola *et al.* (2011) are lower than in the present case (the Strouhal number is approximately 1/10th that of the present case), as are Re and We and no specific information on the forcing amplitude can be deduced, some basic comparisons of the present scenario with figure 14, showing photographs of the jet oscillation, in their work is possible. As has been discussed, the eigenfunctions of the linear model show reasonable agreement with the DNS for $x/D < 20$ for $A = 0.05$. The visual amplitude of the DNS at $x/D = 20$, derived from figure 2, reaches $1.2 y/D$. This amplitude is comparable to that observed in the region around $x_{Tam} = 1500$ in figure 14 (left) of Tammissola *et al.* (2011). Similarly, the amplitude for $A = 0.01$, at $x/D = 20$, where excellent agreement with the DNS is found, reaches $0.6 y/D$, corresponding to the same region in figure 14 (right). As noted by Tammissola *et al.* (2011), the linear analysis around the base flow was obtained far upstream of this region where linear growth could be assumed ($x_{Tam} = 600$). Therefore, the mean flow model of the present work could possibly extend the applicability of linear stability analysis in a similar framework to positions further downstream. However, for larger amplitudes as seen in the lower part of

figure 14 (left), the mean flow model is likely to fail as well. It is worth noting that the growth rates obtained from the DNS and from the mean flow analysis are substantially larger in the near nozzle region than they are in Tammisola *et al.* (2011) ($\max(\alpha_{t,Tam}) = 0.0054$). However, as stated, the growth rates in their analysis were obtained from a position sufficiently far away from the nozzle were growth rates are expectedly smaller than close to the nozzle. In Söderberg (2003) the measured growth rates close to the nozzle are larger than in Tammisola *et al.* (2011) and comparable to the presently obtained growth rates ($\max(\alpha_{t,Söd}) = 0.4$), though the corresponding Strouhal number is approximately 10 times larger than in the present case and Re and We are significantly lower. So, again, no direct comparison is possible. Further, we have checked the influence of using an analytic flow profile as in Tammisola *et al.* (2011) which results in growth rates near the nozzle that are up to 6 times smaller than for the mean flow profile. As discussed in § 3.3, the differences in the growth rates might be attributed to the form of mean flow profiles near the nozzle.

5. Interaction of the fundamental wave with higher harmonics

In the previous section we revealed the potential and limits of the linear stability model in predicting the growth and decay of instability waves. While for $A = 0.01$ very good agreement is found for both, eigenfunctions and growth rates, strong discrepancies are found for $A = 0.05$, which raises the question as to why the linear model fails to predict the stability behaviour of a jet forced with this amplitude. This is in contrast to the single-phase experiments of Oberleithner *et al.* (2014b) where excellent agreement at similar and higher forcing amplitudes was found.

Introducing the Fourier decomposition (4.1) in (3.7), we obtain

$$in\omega\hat{u}_{i,n} + \mathcal{L}_{i,n} = \mathcal{F}_{i,n}^* \tag{5.1}$$

where $\mathcal{L}_{i,n}$ contains the linear terms. Similarly, we have an infinite expansion, governing the harmonics of the flow

$$\mathcal{F}_i = - \sum_{m \neq 0} \frac{\partial}{\partial x_j} (\hat{u}_{i,m} \hat{u}_{j,-m}) - \frac{\partial}{\partial x_j} (\overline{u_i'' u_j''}) \tag{5.2a}$$

$$\mathcal{F}_{i,n}^* = - \sum_{m \neq n,0} \frac{\partial}{\partial x_j} (\hat{u}_{i,m} \hat{u}_{j,n-m}) - \frac{\partial}{\partial x_j} (\widetilde{u_i'' u_j''}) \tag{5.2b}$$

where $\hat{u}_{i,-n} = \hat{u}_{i,n}^*$, with the asterisk denoting the complex conjugate. The fluctuating Reynolds stresses remain small in the present scenario, as is seen by evaluating the turbulent kinetic energy normalised by either the inflow kinetic energy or the coherent kinetic energy (figure 12). In both cases, the fluctuations remain below 1% for most of the domain.

The forcing in (5.2a) is expanded for the respective harmonics as follows:

$$\mathcal{F}_i = - \frac{\partial}{\partial x_j} (\hat{u}_{i,1} \hat{u}_{j,-1} + \hat{u}_{i,-1} \hat{u}_{j,1} + \hat{u}_{i,2} \hat{u}_{j,-2} + \hat{u}_{i,-2} \hat{u}_{j,2}) + \dots \tag{5.3a}$$

$$\mathcal{F}_{i,1}^* = - \frac{\partial}{\partial x_j} (\hat{u}_{i,2} \hat{u}_{j,-1} + \hat{u}_{i,-1} \hat{u}_{j,2} + \hat{u}_{i,3} \hat{u}_{j,-2} + \hat{u}_{i,-2} \hat{u}_{j,3}) + \dots \tag{5.3b}$$

$$\mathcal{F}_{i,2}^* = - \frac{\partial}{\partial x_j} (\hat{u}_{i,1} \hat{u}_{j,1} + \hat{u}_{i,3} \hat{u}_{j,-1} + \hat{u}_{i,-1} \hat{u}_{j,3} + \hat{u}_{i,4} \hat{u}_{j,-2} + \hat{u}_{i,-2} \hat{u}_{j,4}) + \dots \tag{5.3c}$$

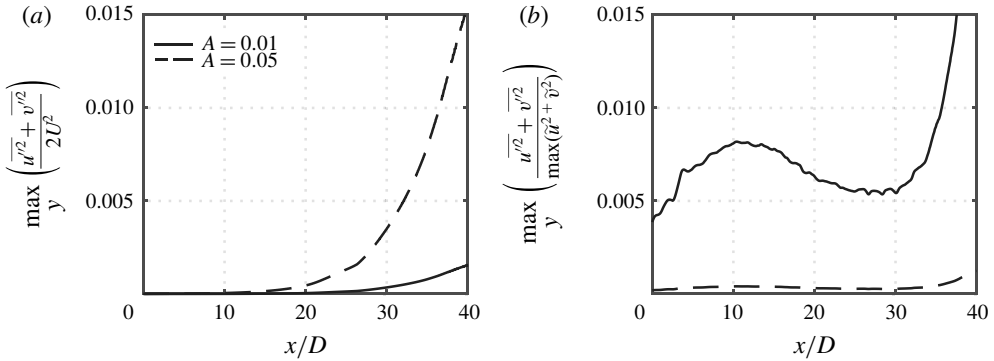


FIGURE 12. Variation of the cross-wise maximum of the total turbulent kinetic energy.

$$\mathcal{F}_{i,3}^* = -\frac{\partial}{\partial x_j} (\hat{u}_{i,1}\hat{u}_{j,2} + \hat{u}_{i,4}\hat{u}_{j,-1} + \hat{u}_{i,-1}\hat{u}_{j,4}) + \dots \tag{5.3d}$$

The terms for $n = 0$ represent the interaction of the fundamental and higher harmonic waves with their respective conjugates, forming a steady flow field which modifies the base flow (which is a solution of the stationary Navier–Stokes equation) towards the mean flow. For the generation of higher harmonics, the following process emerges: the second harmonic is generated by interaction of the fundamental wave with itself and feeds back on the fundamental wave (through interaction with the fundamental wave and higher harmonics), itself and subsequent higher harmonic waves. The third harmonic and subsequent harmonics are generated similarly through interaction of the fundamental wave or higher harmonics with other harmonics. The harmonics themselves are expanded as

$$u_i = \bar{u}_i + \hat{u}_{i,1} + \hat{u}_{i,2} + \hat{u}_{i,3} + \dots \tag{5.4}$$

As noted by Turton, Tuckerman & Barkley (2015), the harmonics then often decay as $\hat{u}_{i,n} \propto O(\epsilon^n)$ where ϵ is the amplitude of the fundamental mode. Given the assumption holds for the present case, when investigating equation (5.1), it should hold that $\mathcal{F}_{i,1}^* \propto O(\epsilon^3)$ while $\mathcal{L}(u_{i,1}) \propto O(\epsilon)$. Further it is then required that the amplitude of second harmonic is (at least) approximately an order of magnitude weaker than that of the fundamental mode.

In the body of literature regarding mean flow stability analysis, a number examples are found where the mean flow model fails to accurately predict the evolution of the fundamental mode of the flow. For instance, Sipp & Lebedev (2007) performed a weakly nonlinear analysis of a cylinder wake and an open cavity flow and determined which contributions to the nonlinear terms had to be retained in order to fulfil the marginal stability criterion of the mean flow. While they found excellent agreement for the cylinder wake, a similar analysis of the cavity flow revealed the mean flow to remain strongly unstable. Similarly, Turton *et al.* (2015) found a disagreement for the case of a standing wave in thermosolutal convection. In these cases, failure of the mean flow model is due to a strong nonlinear interaction of the first and second harmonic such that $\mathcal{F}_{i,1}^*$ is not small. In Boujo, Bauerheim & Noiray (2018) the study of linear response to harmonic forcing of a shear layer over a cavity revealed good agreement with a corresponding large eddy simulation, despite a non-negligible

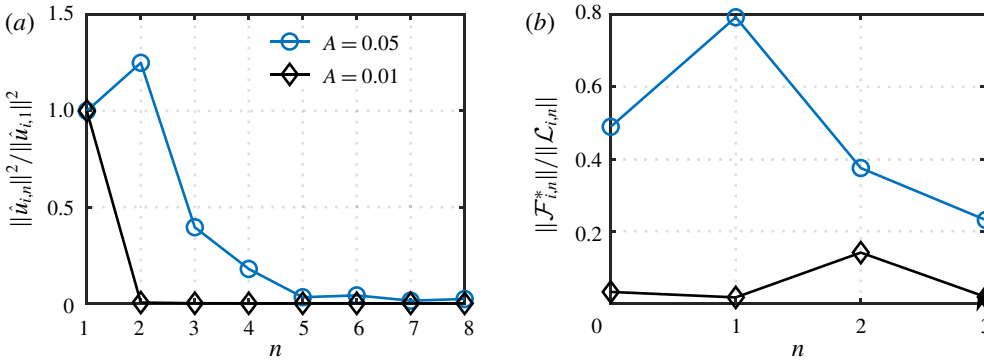


FIGURE 13. Ratio of the energy of the harmonics to the energy of the fundamental wave (a) and the ratio of nonlinear to linear terms in (5.3) (b).

influence of the second harmonic, i.e. $\|\hat{u}_{i,1}\| \gg \|\hat{u}_{i,2}\|$. This is attributed to small interaction of the second harmonic with the fundamental wave. The nonlinear modification of the mean flow is also the basis for a self-consistent model, proposed by Mantič-Lugo, Arratia & Gallaire (2014), which retains the nonlinear forcing of the fundamental wave on the mean flow, in order to iteratively (without *a priori* knowledge of the mean flow) obtain stability properties of a cylinder wake, by requiring the resulting mean flow to be marginally stable. In the light of these findings, we investigate the development of higher harmonic waves in the present flow for $A = 0.01$ and $A = 0.05$, based on the results of the DNS to pinpoint possible reasons for the failure of the linear model for stronger forcings.

We inspect the energy ratio of the fundamental wave and higher harmonics by their respective matrix norms, induced by the Euclidean norm, in figure 13(a). A clear separation between the fundamental wave and the second harmonic is seen for $A = 0.01$ (the ratio of the respective norms is of almost 16). For $A = 0.05$ this separation is lost, with the second harmonic being even more energetic than the fundamental wave (the ratio of the norms is 0.9).

To get a more direct view on the growth of the harmonic waves, we compute their amplitudes from (4.2). They are shown in figure 14. All amplitudes are normalised with respect to the initial value of the fundamental wave at $x = 0$. For $A = 0.01$ the fundamental wave saturates around $x/D = 20$ and starts decaying shortly thereafter, reaching a maximum gain of approximately 25. The second and third harmonics saturate further downstream around $x/D = 25$ and reach a maximum gain of approximately 0.5 and 0.25, respectively. Again a clear separation is evident, as the gain of the fundamental mode is higher by a factor of 50, respectively 100. At a forcing amplitude $A = 0.05$, the maximum gain of the fundamental wave is slightly reduced to around 24 and the point of saturation is shifted upstream to around $x/D = 19$. In contrast to $A = 0.01$ the saturation level is sustained much longer and the wave starts decaying only after $x/D = 30$. As expected, the growth of the second and third harmonics is dramatically increased, reaching gains of approximately 43 and 16 respectively. Both waves saturate at around $x/D = 28$. Hence, the gain of the fundamental wave exceeds that of the second and third harmonic by a factor of 0.56 and 1.5 respectively.

The influence of the quadratic nonlinearities $\mathcal{F}_{i,n}^*$ is shown in figure 13(b). They are evaluated using the terms displayed in (5.3). For $A = 0.01$, they are dominated by

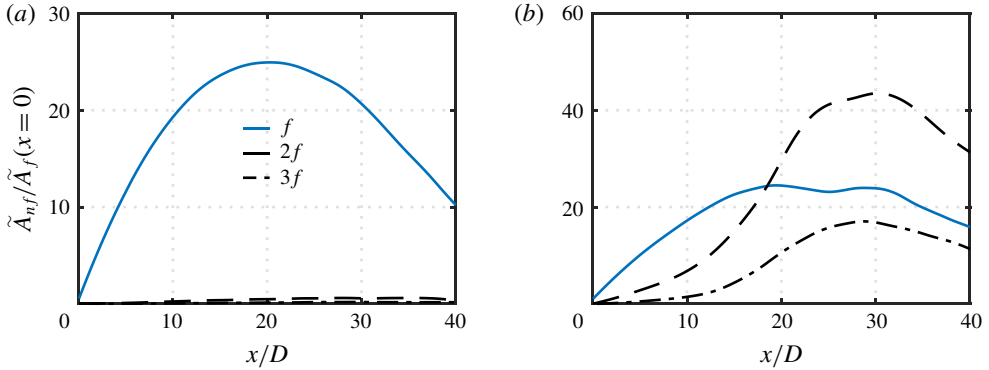


FIGURE 14. Amplitudes \tilde{A}_n of the fundamental wave and its higher harmonics for (a) $A = 0.01$, (b) $A = 0.05$.

	$A = 0.01$	$A = 0.05$
$\ \partial x_j(\hat{u}_{i,1}\hat{u}_{j,-1} + \hat{u}_{i,-1}\hat{u}_{j,1})\ /\ \mathcal{L}_{i,0}\ $	0.1022	0.2356
$\ \partial x_j(\hat{u}_{i,2}\hat{u}_{j,-2} + \hat{u}_{i,-2}\hat{u}_{j,2})\ /\ \mathcal{L}_{i,0}\ $	0.0014	0.3481
$\ \partial x_j(\hat{u}_{i,3}\hat{u}_{j,-3} + \hat{u}_{i,-3}\hat{u}_{j,3})\ /\ \mathcal{L}_{i,0}\ $	0.0005	0.0983
$\ u_{i,b} - \bar{u}_i\ /\ u_{i,b}\ $	0.0774	0.7288

TABLE 5. Influence of the quadratic harmonic interactions in the mean flow equation and mean flow correction. The quasi-stationary solution of the unforced flow is taken as the base flow $u_{i,b}$.

the first and second term for $n = 0, 1$ and the first term for $n = 2, 3$. For $A = 0.05$ all displayed terms have non-negligible contributions. For $A = 0.01$, the influence of $\mathcal{F}_{i,1}^*$ is negligible ($\mathcal{F}_{i,1}^* \propto O(\epsilon^3)$), leaving the dynamics of the fundamental wave unaffected by higher harmonic interaction. In contrast, for $A = 0.05$, the influence is profound and the nonlinear modification to the fundamental wave even exceeds that of the mean flow ($\mathcal{F}_{i,1}^* \gg O(\epsilon^3)$). Interestingly, for $A = 0.01$, $\mathcal{F}_{i,2}^*$ is non-negligible and exceeds the zero-order terms, which is in contrast to the findings of Turton *et al.* (2015), who argued that $\partial/\partial x_j(\hat{u}_{i,1}\hat{u}_{j,1})$ (which generates $u_{i,2}$) should be small compared to $\partial/\partial x_j(\hat{u}_{i,1}\hat{u}_{j,-1} + \hat{u}_{i,-1}\hat{u}_{j,1})$. However, since from (5.4) it should hold that $\mathcal{F}_{i,2}^* \propto O(\epsilon^2)$ and $\mathcal{L}(u_{i,2}) \propto O(\epsilon^2)$, this does not violate our assumption. In summary, two main effects are observed that likely lead to failure of the mean flow stability model for $A = 0.05$: the missing spectral energy separation of the second (and third) harmonic compared to the fundamental wave and the nonlinear modification of the fundamental wave through harmonic–fundamental/harmonic–harmonic interaction, which is explicitly violating the assumption we have made for the mean flow analysis in § 3.1.

The influence of the harmonic interactions on the mean flow is assessed in table 5. The mean flow correction for $A = 0.01$ is generally small and solely dominated by the fundamental wave, whereas for $A = 0.05$, significant influence of the second and also third harmonic is observed. To get a clearer picture of the spatial development of the mean flow forcing, the energy transfer between the mean field and the harmonic–harmonic interactions is investigated. Following Reynolds & Hussain (1972)

and Oberleithner *et al.* (2014b), by neglecting any viscous involvement, the energy equation for the mean flow across both fluid phases can be stated as

$$\frac{1}{2} \frac{d}{dx} \int_0^\infty \bar{u}^3 dy \approx - \sum_{n=0}^\infty \underbrace{\left(\int_0^\infty -\hat{u}_n \hat{v}_n^* \frac{\partial \bar{u}}{\partial y} dy \right)}_{\mathcal{P}_n} - \int_0^\infty -\overline{u''v''} \frac{\partial \bar{u}}{\partial y} dy, \quad (5.5)$$

where only terms dominating the balance have been retained and the coherent term is expanded as in (5.3a). The first term on the right-hand side refers to the energy production by action of the mean field on the coherent Reynolds stresses, while the second term accounts similarly for the energy production by action of the mean field on the fluctuating Reynolds stresses.

The streamwise contributions of the coherent production terms \mathcal{P}_n are given in figure 15. Since the fluctuations are very small, they are, again, neglected. Further, the production for $A = 0.01$ is essentially limited to the fundamental wave and therefore is not further discussed. The balance is dominated by the energy production of the fundamental wave, which draws energy from the mean field (since it is positive) throughout the domain and reaches its maximum at $x/D = 22$ shortly downstream of the saturation point of the fundamental wave \mathcal{P}_1 . The energy that is fed to the now saturated fundamental wave is distributed on the higher harmonics that are still growing as seen in figure 14. The value of \mathcal{P}_2 is always negative, and thus continuously transferring energy back to the mean flow; \mathcal{P}_3 is positive for $15 < x/D < 25$ and peaks around the same position as the fundamental wave. For $x/D > 22$ the contributions \mathcal{P}_1 and \mathcal{P}_3 diminish and \mathcal{P}_3 becomes negative as well.

It might seem counter-intuitive that the production of the fundamental wave is significantly larger than that of the second harmonic, whereas, for the harmonics themselves and their self-interaction on the mean flow, the second harmonic dominates. Indeed, for the normal Reynolds stresses the dominating influence is that of the second harmonic. However, for the tangential stresses, the contribution of the fundamental mode is largest. Since, $\partial \bar{u} / \partial y \gg \partial \bar{u} / \partial x \approx \partial \bar{v} / \partial y \approx \partial \bar{v} / \partial x$, the tangential stresses dominate \mathcal{P} .

The negative production in \mathcal{P}_2 , \mathcal{P}_3 corresponds to a reversed energy cascade from small scale oscillations to the large scale mean flow. It was hypothesised by Oberleithner *et al.* (2014b) that, while such a reversed energy cascade is acting, there is no linear dependency between the mean field and the coherent motion which could lead to a breakdown of the linear stability model. In the present case, although \mathcal{P}_1 remains positive, \mathcal{P}_2 is increasingly feeding energy back to the mean flow during the growth phase of the forced instability wave, while having a profound influence on the systems stability behaviour, as is evident from its gain. It therefore seems possible that the reversed energy cascade, caused by modification of the mean flow through the second harmonic, is another cause for the breakdown of the stability model for $A = 0.05$.

The present work solely focuses on modal growth to explain the developing instabilities. It is possible that non-modal growth, caused by non-orthogonality of the eigenvectors, has an influence on the short-time behaviour of the forced jet and, if significant, possibly could explain some of the shortcomings of the linear stability analysis. There have been some studies on transient growth on two-phase mixing layers and jets by e.g. Yecko & Zaleski (2005) and De Luca (2001). In both studies a possibility of transient growth in the respective flows was found, however, no

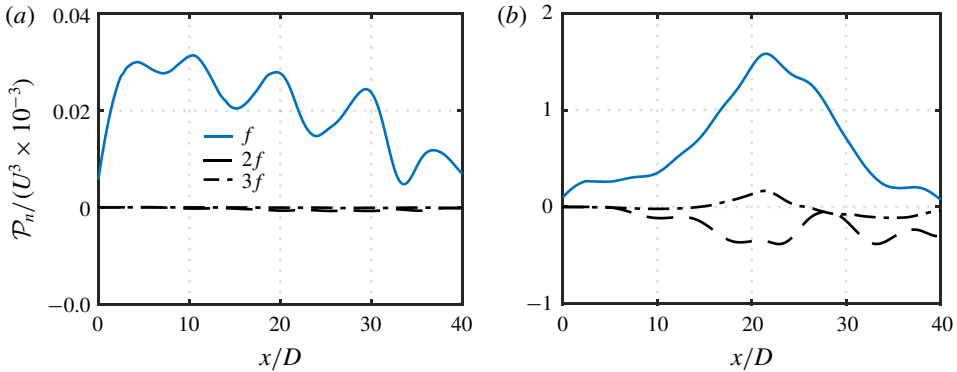


FIGURE 15. Energy production \mathcal{P}_n of the fundamental wave and its higher harmonics for (a) $A = 0.01$, (b) $A = 0.05$.

validation using experimental or numerical data has been conducted and it remains unknown whether these effects actually have significant influence on the flow.

From a phenomenological viewpoint, the strong involvement of the higher harmonics can be attributed to the formation of vortical structures, observed in the gas phase around the oscillating jet. Further, while due to the transverse forcing at the inlet, the fundamental mode is sinuous, the second harmonic wave is dilatational as can be deduced from the display of the higher harmonic waves in appendix G. Similar findings of a strong interaction between the sinuous fundamental wave and a dilatational second harmonic are given by Mehring & Sirignano (1999) and Clark & Dombrowski (1972). The superposition of both modes leads to characteristic agglomeration of liquid along the wave crests and thinning along the jet axis as seen in figure 2(b).

5.1. Vorticity dynamics

The evolution of vortical structures shown in figure 4 shows increasingly complex patterns, starting with an initial vorticity sheet close to the inlet that develops into discrete vortical structures with subsequent interaction and roll-up in the enlarging wave troughs of the unstable liquid jet. Detailed numerical studies of liquid jets by Jarrahbashi & Sirignano (2014) and Zandian, Sirignano & Hussain (2018) show significant interaction between vortex and interface dynamics in the process of interface deformation and breakup. To investigate the vorticity generation we evaluate the terms in the vorticity equation of an incompressible fluid

$$\frac{\partial \Omega_i}{\partial t} + u_j \frac{\partial \Omega_i}{\partial x_j} = \Omega_j \frac{\partial u_i}{\partial x_j} + \frac{1}{\rho^2} \epsilon_{ijk} \frac{\partial \rho}{\partial x_j} \frac{\partial p}{\partial x_k} + \nu \frac{\partial^2 \Omega_i}{\partial x_j^2}, \quad (5.6)$$

where the terms on the right-hand side correspond to vortex stretching or tilting by velocity gradients, the baroclinic torque and vorticity diffusion. In two-dimensional flows the vorticity reduces to a scalar quantity and vortex stretching or tilting is absent so that the vorticity equation reduces to

$$\frac{\partial \Omega}{\partial t} + u \frac{\partial \Omega}{\partial x} + v \frac{\partial \Omega}{\partial y} = \frac{1}{\rho^2} \left(\frac{\partial \rho}{\partial x} \frac{\partial p}{\partial y} - \frac{\partial \rho}{\partial y} \frac{\partial p}{\partial x} \right) + \nu \left(\frac{\partial^2 \Omega}{\partial x^2} + \frac{\partial^2 \Omega}{\partial y^2} \right). \quad (5.7)$$

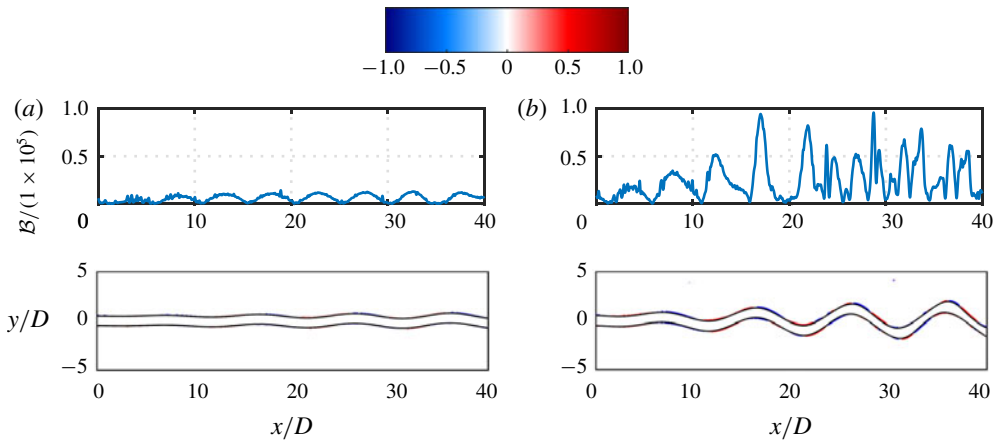


FIGURE 16. Instantaneous, cross-wise integrated baroclinic vorticity \mathcal{B} and snapshot of the corresponding field normalised by its maximum for (a) $A = 0.01$, (b) $A = 0.05$.

As shown by Jarrahbashi & Sirignano (2014), the baroclinic term dominates for large density ratios. Their results are in line with observations from experimental investigations of liquid jets in high-velocity gas co-flow by Marmottant & Villermaux (2004). They found that while primary destabilisation of the interface is due to Kelvin–Helmholtz-type shear instabilities, at later stages when the interface is significantly corrugated, secondary instabilities evolve which they attribute to Rayleigh–Taylor type baroclinic instabilities. In the present work the transverse oscillation of the jet induces an acceleration of the interface perpendicular to the jet axis. Together with the curved interface this leads to a misalignment of pressure and density gradients. As a result the baroclinicity along the interface is expected to grow in downstream direction.

The normalised, instantaneous streamwise development of the baroclinicity, integrated across the jet

$$\mathcal{B}(x, t) = \frac{D}{U^2} \int_0^\infty \left| \frac{(\nabla \rho \times \nabla p)}{\rho^2} \right| dy, \tag{5.8}$$

is given in figure 16. As can be seen, the term varies periodically with half the wavelength of the forced oscillation at a relatively steady amplitude throughout the domain for $A = 0.01$. For $A = 0.05$ the term shows a significant downstream growth and becomes highly irregular for $x/D > 20$ with peaks which are approximately a factor 5 larger than the initial amplitude.

From the viewpoint of instability waves, the increase in baroclinicity coincides with the growth of the higher harmonic waves analysed in § 5. In fact, the Fourier transformation of \mathcal{B} shown in figure 18 expectedly shows the fundamental frequency at twice the frequency of the forced oscillation. However, from the streamwise evolution of the harmonics it is evident that the energy content of the second harmonic exceeds that of the fundamental frequency for $22 < x < 30$ of the nonlinear region which concurs with the qualitative development of the harmonics in § 5. This suggests that the steep increase in baroclinicity is linked to the growth of higher harmonic waves in the unstable jet.

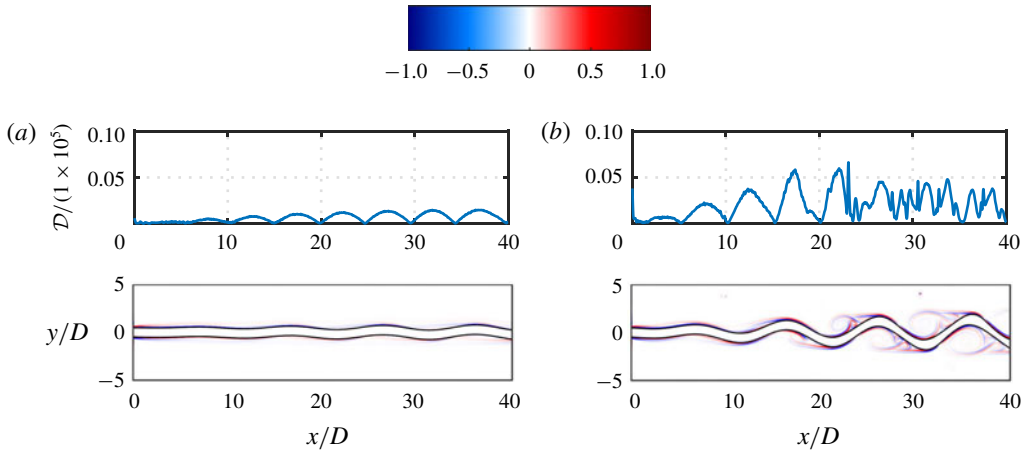


FIGURE 17. Instantaneous, cross-wise integrated vorticity dissipation \mathcal{D} and snapshot of the corresponding field normalised by its maximum for (a) $A = 0.01$, (b) $A = 0.05$.

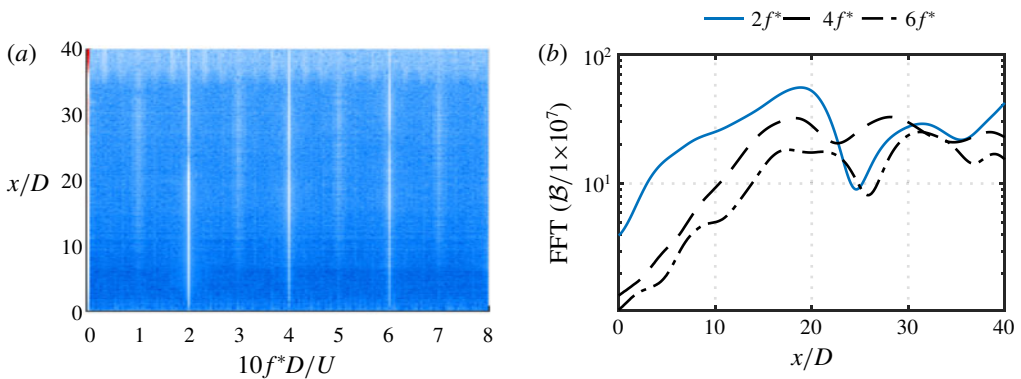


FIGURE 18. Streamwise evolution of the Fourier decomposition of the cross-wise-averaged baroclinic vorticity for $A = 0.05$. The spectrum along the streamwise coordinate is shown (a) as well as the streamwise development of the energy of the first three harmonics (b).

For completeness the viscous dissipation of vorticity

$$\mathcal{D}(x, t) = \frac{D}{U^2} \int_0^\infty |v \Delta \Omega| dy \tag{5.9}$$

is shown in figure 17. Its qualitative streamwise development is comparable to that of the baroclinicity, although its influence is considerably weaker, given that values of the baroclinicity are around an order of magnitude larger. Additionally, its growth within the nonlinear region is not as pronounced as for the baroclinicity.

6. Summary and conclusions

The linear and nonlinear stability of a transversely forced planar liquid jet in a still ambient gas is studied using nonlinear numerical simulation and local linear stability

analysis, based on a time-averaged mean flow representation of the unsteady nonlinear flow.

The simulated jet, with a $Re_l = 8962$ and $We = 440$, is forced at two forcing amplitudes $A = 0.01, 0.05$. The forcing produces an initially monochromatic instability wave that grows in space until it saturates and decays.

For the linear stability model, the time-averaged mean flow is obtained from the nonlinear simulation. Due to the non-parallelism of the forced flow, a mass-conserving model is proposed to account for the spreading of the interface position in the mean flow.

General stability properties are derived, based on the unforced flow, for a wide range of frequencies. Two unstable modes are found of which mode I is relevant for the present forcing cases. The modes vaguely correspond to the modes I and II found by Söderberg (2003). By analysing the energy budget of mode I it is found that the instability is mainly driven by the viscosity defect of the adjacent fluid streams in the shear layer.

Detailed comparison of the stability model using the forced mean flow with the DNS shows excellent agreement for $A = 0.01$ and the proposed interface correction results in an improved replication of the transverse shear layer spreading in the eigenfunctions. Also, without correction the position of the neutral point is somewhat over-predicted. For $A = 0.05$, significant deviations in the eigenfunctions for $x/D > 20$ are observed. The linear model completely fails to predict correct growth rates for this forcing amplitude.

Reasons for the failure of the linear model at $A = 0.05$ are found by analysis of higher harmonic wave growth in the flow. While for $A = 0.01$ the fundamental wave dominates the stability behaviour, for $A = 0.05$ significant influence of the second and third harmonics is observed. The second harmonic thereby reaches gain levels exceeding that of the fundamental wave. As a result, the fundamental wave exhibit strong nonlinear modification through higher harmonics which explains the failing of the linear model. Similar limitations to mean flow stability have been revealed by Sipp & Lebedev (2007) and Turton *et al.* (2015).

In conclusion, the linear stability model performs well for low forcing amplitudes over the whole spatial extent, even in the presence of moderate nonlinear effects. The inclusion of a mean interface correction scheme has proven to increase reliability of the mean flow based linear stability model. These results are in line with the conclusions drawn by Oberleithner *et al.* (2014b). However, strong discrepancies arise for stronger forcings when nonlinear interactions between the fundamental mode and higher-order modes significantly alter the flow. From the viewpoint of vorticity dynamics, the higher harmonic waves correspond to a substantial growth of baroclinic vorticity along the liquid/gas interface.

Appendix A. Derivation of the conditions for stress continuity

For an incompressible Newtonian fluid, the stress tensor of each fluid phase is written as

$$S_{ij,l,g}^* = p_{l,g}^* \delta_{ij} + \mu_{l,g} \left(\frac{\partial u_{i,l,g}^*}{\partial x_j^*} + \frac{\partial u_{j,l,g}^*}{\partial x_i^*} \right). \tag{A 1}$$

The stars indicate dimensioned quantities. To obtain the normal and tangential components of (A 1), we need the unit normal vector of the interface which is given as

$$n_i^* = \frac{\nabla \tilde{H}^*}{|\nabla \tilde{H}^*|} = \frac{-(\partial \tilde{h}^* / \partial x^*, 1)^T}{\sqrt{(\partial \tilde{h}^* / \partial x^*)^2 + 1}}, \tag{A 2}$$

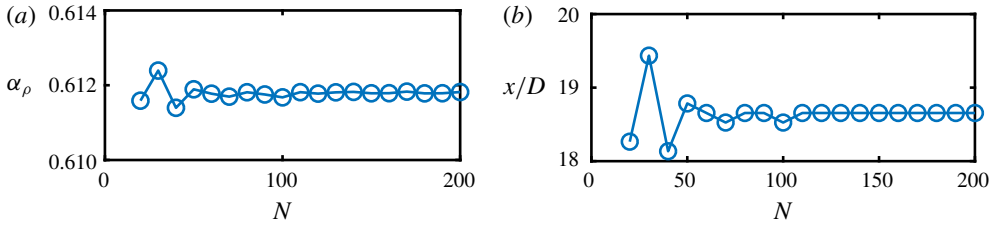


FIGURE 19. Convergence of the real part of the traced eigenvalue, α_ρ , at the neutral point and position of the neutral point, x/D , for various numbers, N , of collocation points.

where $\tilde{H}^*(x, y, t) = y^* - \tilde{h}^*(x, t) = 0$ is the curve defining the interface. For small surface displacements, we neglect quadratic terms of disturbed quantities and arrive at $n_i^* = (-\partial\tilde{h}^*/\partial x^*, 1)^T$. The tangent vector is readily given as $t_i^* = (1, \partial\tilde{h}^*/\partial x^*)^T$.

The continuity of shear stress is given as $t_i^* S_{ij,l}^* n_j^* = t_i^* S_{ij,g}^* n_j^*$. Inserting the decomposition (3.4) (neglecting the fluctuations), using Taylor expansion of $h^*(x^*, t^*)$ around $y^* = \tilde{h}^*$ and neglecting quadratic terms of disturbed quantities, we obtain

$$\mu_l \left[\frac{\partial \tilde{v}}{\partial x} + \frac{\partial \tilde{u}}{\partial y} + \tilde{h} \frac{d^2 \tilde{u}}{dy^2} \right]_{y=\tilde{h},l}^* - \mu_g \left[\frac{\partial \tilde{v}}{\partial x} + \frac{\partial \tilde{u}}{\partial y} + \tilde{h} \frac{d^2 \tilde{u}}{dy^2} \right]_{y=\tilde{h},g}^* = 0. \tag{A 3}$$

Dividing by $\mu_l U/D$ we arrive at the dimensionless form

$$\left[\frac{\partial \tilde{v}}{\partial x} + \frac{\partial \tilde{u}}{\partial y} + \tilde{h} \frac{d^2 \tilde{u}}{dy^2} \right]_{y=\tilde{h},l} - m \left[\frac{\partial \tilde{v}}{\partial x} + \frac{\partial \tilde{u}}{\partial y} + \tilde{h} \frac{d^2 \tilde{u}}{dy^2} \right]_{y=\tilde{h},g} = 0, \tag{A 4}$$

where $m = \mu_g/\mu_l$.

Similarly, the continuity of normal stress is given as $n_i^* S_{ij,l}^* n_j^* = n_i^* S_{ij,g}^* n_j^* - \sigma \partial n_i^*/\partial x^*$. Using Taylor expansion again and dividing by $\rho_l U^2/D$ we get

$$\left[\tilde{p} - \frac{2}{Re_l} \frac{\partial \tilde{v}}{\partial y} \right]_{y=\tilde{h},l} - \left[r\tilde{p} - \frac{2m}{Re_l} \frac{\partial \tilde{v}}{\partial y} \right]_{y=\tilde{h},g} + \frac{1}{We} \frac{\partial^2 \tilde{h}}{\partial x^2} = 0. \tag{A 5}$$

Appendix B. Convergence analysis of the linear stability model

A convergence analysis, to estimate the necessary number of collocation points, is performed at the point of neutral stability for the varying interface model with $A = 0.01$. The number of collocation points is successively increased from $N = 20$ to $N = 200$ points in each phase. The convergence of the streamwise position of the neutral point and the corresponding real part of the eigenvalue, α_ρ , is shown in figure 19. As is seen, the choice of $N = 110$ is adequate.

Appendix C. Flow conditions of the two-layer Poiseuille flow by Dongarra *et al.* (1996)

Dongarra *et al.* (1996) computed unstable eigenvalues for a two-layer plane Poiseuille flow that is used for validating the present two-phase linear stability solver. The flow conditions are restated here for convenience. The basic flow is

$$u_1(y) = A_1 y^2 + a_1 y + 1, \quad -1 < y < 0, \tag{C 1}$$

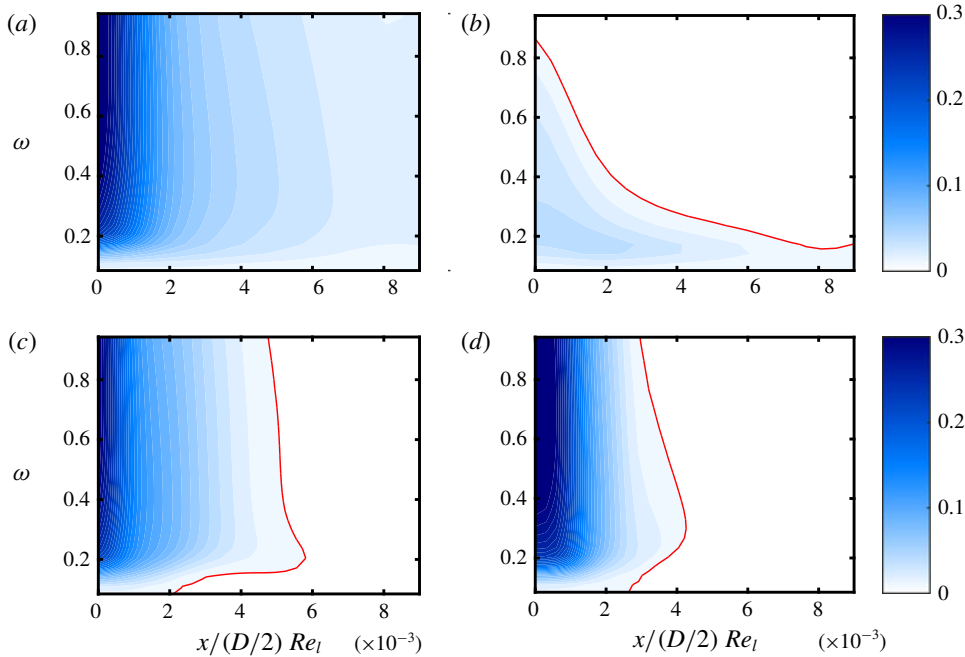


FIGURE 20. Stability map for the base flow model: mode I (a), mode II (b), fixed interface model (mode I) at $A=0.01$ (c), varying interface model (d). Shown is the spatial growth rate $-\alpha_i D/2$ and the curve indicating neutral stability, i.e. $\alpha_i D/2=0$, in red. The axes scaling is as in Söderberg (2003), where $\omega = \pi f D/U$.

$$u_2(y) = A_2 y^2 + a_2 y + 1, \quad 0 < y < n, \tag{C 2}$$

where

$$A_1 = \frac{-(m+n)}{n(n+1)}, \quad a_1 = \frac{n^2 - m}{n(n+1)}, \quad A_2 = \frac{A_1}{m}, \quad a_2 = \frac{a_1}{m}. \tag{C 3a-d}$$

The viscosity ratio is $m = \mu_2/\mu_1 = 2$, the depth ratio is $n = d_2/d_1 = 1.2$, where d denotes the extend of the respective domains. The density ratio is $r = 1$ and the surface tension is $\sigma = 0$. The obtained eigenvalues using temporal analysis with $\alpha = 1$ are stated in table 3.

Appendix D. Stability maps with the scaling of Söderberg (2003)

The stability maps, derived in § 3.4, are reprinted here using the axes scaling of Söderberg (2003) for direct comparison (figure 20).

Appendix E. The energy budget for spatial modes in two-phase flows

Closely following Boomkamp & Miesen (1996) and Otto (2012), a balance for the coherent kinetic energy $\tilde{u}_i \tilde{u}_i$ in each fluid phase is obtained by taking the inner product of (3.7) with \tilde{u}_i . Upon averaging over one period, $\gamma = 2\pi/\omega$, integrating along y and by adding the results over both fluid phases, equation (3.21) is obtained.

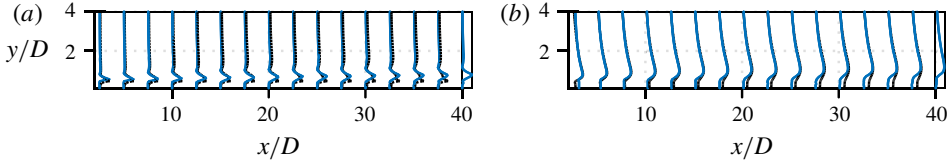


FIGURE 21. Comparison of the computed amplitude functions, normalised by their maximum value, from the base flow model and the DNS for $A = 0.01$, (a) \hat{u} ; (b) \hat{v} . Blue lines show the DNS while black lines show the LSA.

The respective terms on the right-hand side of the equation are given as

$$\begin{aligned} \text{MFL}_l &= \frac{1}{\gamma} \frac{\partial}{\partial x} \int_0^\gamma \int_0^D \left[\frac{\bar{u}_l}{2} (\tilde{u}_l + \tilde{v}_l) + \tilde{u}_l \tilde{p}_l \right. \\ &\quad \left. - \frac{1}{Re_l} \left(2\tilde{u}_l \frac{\partial \tilde{u}_l}{\partial x} + \tilde{v}_l \frac{\partial \tilde{u}_l}{\partial y} + \tilde{v}_l \frac{\partial \tilde{v}_l}{\partial y} \right) \right] dy dt, \end{aligned} \quad (\text{E } 1a)$$

$$\begin{aligned} \text{MFL}_g &= \frac{1}{\gamma} \frac{\partial}{\partial x} \int_0^\gamma \int_D \left[\frac{r\bar{u}_g}{2} (\tilde{u}_g + \tilde{v}_g) + r\tilde{u}_g \tilde{p}_g \right. \\ &\quad \left. - \frac{m}{Re_l} \left(2\tilde{u}_g \frac{\partial \tilde{u}_g}{\partial x} + \tilde{v}_g \frac{\partial \tilde{u}_g}{\partial y} + \tilde{v}_g \frac{\partial \tilde{v}_g}{\partial y} \right) \right] dy dt, \end{aligned} \quad (\text{E } 1b)$$

$$\text{DIS}_l = \frac{1}{\gamma} \frac{1}{Re_l} \int_0^\gamma \int_0^D \left[2 \left(\frac{\partial \tilde{u}_l}{\partial x} \right)^2 + \left(\frac{\partial \tilde{u}_l}{\partial y} + \frac{\partial \tilde{v}_l}{\partial x} \right)^2 + 2 \left(\frac{\partial \tilde{v}_l}{\partial y} \right)^2 \right] dy dt, \quad (\text{E } 2a)$$

$$\text{DIS}_g = \frac{1}{\gamma} \frac{m}{Re_l} \int_0^\gamma \int_D \left[2 \left(\frac{\partial \tilde{u}_g}{\partial x} \right)^2 + \left(\frac{\partial \tilde{u}_g}{\partial y} + \frac{\partial \tilde{v}_g}{\partial x} \right)^2 + 2 \left(\frac{\partial \tilde{v}_g}{\partial y} \right)^2 \right] dy dt, \quad (\text{E } 2b)$$

$$\text{REY}_l = \frac{1}{\gamma} \int_0^\gamma \int_0^D \left[(-\tilde{u}_l \tilde{v}_l) \frac{\partial \bar{u}_l}{\partial x} \right] dy dt, \quad (\text{E } 3a)$$

$$\text{REY}_g = \frac{1}{\gamma} r \int_0^\gamma \int_D \left[(-\tilde{u}_g \tilde{v}_g) \frac{\partial \bar{u}_g}{\partial x} \right] dy dt, \quad (\text{E } 3b)$$

$$\text{TAN} = \frac{1}{\gamma} \frac{1}{Re_l} \int_0^\gamma \left[m \left(\frac{\partial \tilde{u}_l}{\partial y} + \frac{\partial \tilde{v}_l}{\partial x} \right) \tilde{u}_l - \left(\frac{\partial \tilde{u}_g}{\partial y} + \frac{\partial \tilde{v}_g}{\partial x} \right) \tilde{u}_g \right]_{y=\bar{h}} dt, \quad (\text{E } 4a)$$

$$\text{NOR} = \frac{1}{\gamma} \int_0^\gamma \left[\left(r\tilde{p}_l + \frac{2m}{Re_l} \frac{\partial \tilde{v}_l}{\partial y} \right) \tilde{v}_l - \left(\tilde{p}_g + \frac{2}{Re} \frac{\partial \tilde{v}_g}{\partial y} \right) \tilde{v}_g \right]_{y=\bar{h}} dt. \quad (\text{E } 4b)$$

Appendix F. Comparison of DNS and the base flow model

For completeness, we briefly present the results of §4 for the base flow model and the DNS ($A = 0.01$) here. In figure 21, the streamwise comparison of the eigenfunctions is shown. The growth rates and phase velocities are compared in figure 22. The results corroborate the advantage of the mean flow model. During the downstream development of the jet increasing discrepancies between the DNS and the LSA are evident from the eigenfunction profiles, as the mean flow spreading, induced by the oscillation is not taken into account in the base flow. As a result, no point of neutral stability is predicted (as already evident from figure 8a), and growth rates are generally overpredicted. Similar results are seen for the phase velocity.

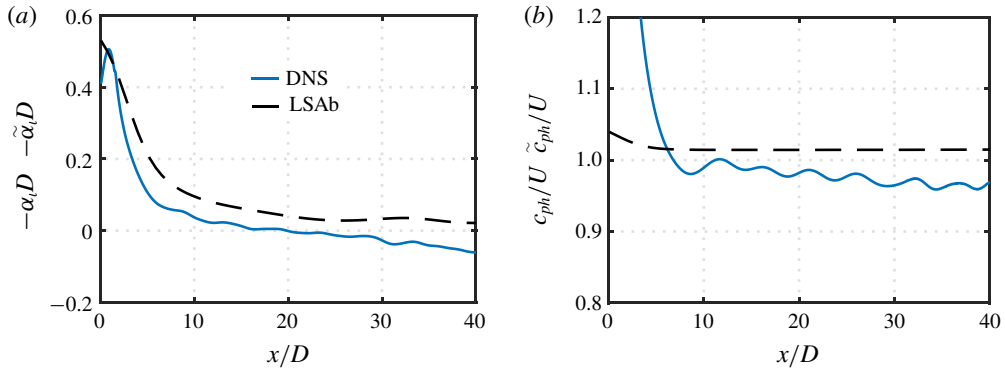


FIGURE 22. Comparison of the computed growth rates $-\alpha_t D$ from the linear stability model and $-\tilde{\alpha}_t D$ the DNS (a) and phase velocities c_{ph}/U , \tilde{c}_{ph}/U (b) for $A=0.01$.

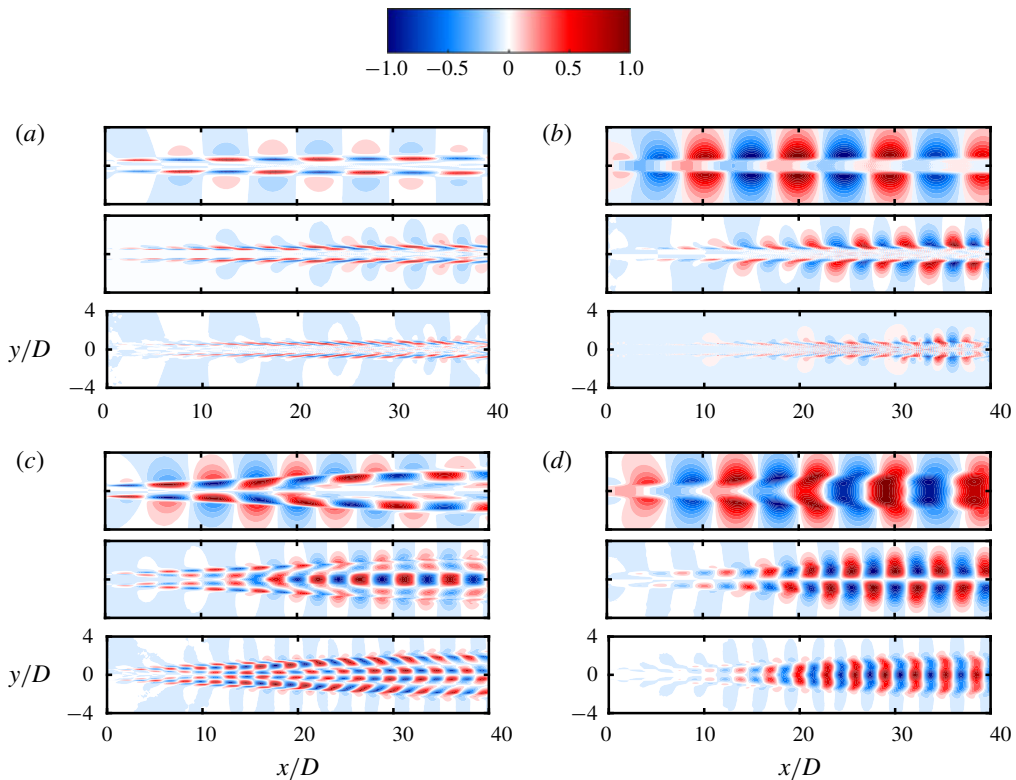


FIGURE 23. Real part of the fundamental, second and third harmonic waves (top to bottom in each panel) for (a) $A=0.01$, \hat{u} ; (b) $A=0.01$, \hat{v} ; (c) $A=0.05$, \hat{u} ; (d) $A=0.05$, \hat{v} . Note that each mode and component is normalised individually by its maximum for improved readability.

Appendix G. Illustration of the Fourier modes

The higher harmonic waves, derived from the Fourier decomposition (4.1) of the velocity field, are displayed here for further clarification (figure 23).

REFERENCES

- BARKLEY, D. 2006 Linear analysis of the cylinder wake mean flow. *Europhys. Lett.* **75** (5), 750–756.
- BENEDDINE, S., SIPP, D., ARNAULT, A., DANDOIS, J. & LESSHAFFT, L. 2016 Conditions for validity of mean flow stability analysis. *J. Fluid Mech.* **798**, 485–504.
- BOBUSCH, B. C., WOSZIDLO, R., BERGADA, J. M., NAYERI, C. N. & PASCHEREIT, C. O. 2013 Experimental study of the internal flow structures inside a fluidic oscillator. *Exp. Fluids* **54** (6), 1559.
- BOECK, T. & ZALESKI, S. 2005 Viscous versus inviscid instability of two-phase mixing layers with continuous velocity profile. *Phys. Fluids* **17** (3), 032106.
- BOOMKAMP, P. A. M. & MIESEN, R. H. M. 1996 Classification of instabilities in parallel two-phase flow. *Intl J. Multiphase Flow* **22**, 67–88.
- BOUJO, E., BAUERHEIM, M. & NOIRAY, N. 2018 Saturation of a turbulent mixing layer over a cavity: response to harmonic forcing around mean flows. *J. Fluid Mech.* **853**, 386–418.
- BRACKBILL, J. U., KOTHE, D. B. & ZEMACH, C. 1992 A continuum method for modeling surface tension. *J. Comput. Phys.* **100** (2), 335–354.
- CHEUNG, L. C. & ZAKI, T. A. 2010 Linear and nonlinear instability waves in spatially developing two-phase mixing layers. *Phys. Fluids* **22** (5), 052103.
- CLARK, C. J. & DOMBROWSKI, N. 1972 Aerodynamic instability and disintegration of inviscid liquid sheets. *Proc. R. Soc. Lond. A* **329** (1579), 467–478.
- COHEN, J. & WYGNANSKI, I. 1987 The evolution of instabilities in the axisymmetric jet. Part 1. The linear growth of disturbances near the nozzle. *J. Fluid Mech.* **176**, 191–219.
- CRIGHTON, D. G. & GASTER, M. 1976 Stability of slowly diverging jet flow. *J. Fluid Mech.* **77** (2), 397–413.
- CUMMINS, S. J., FRANCOIS, M. M. & KOTHE, D. B. 2005 Estimating curvature from volume fractions. *Comput. Struct.* **83** (6), 425–434.
- DE LUCA, L. 2001 Non-modal growth of disturbances in free-surface flows. In *Proceedings of International Conference RDAMM-2001*, vol. 6.
- DELBENDE, I., CHOMAZ, J. & HUERRE, P. 1998 Absolute/convective instabilities in the batchelor vortex: a numerical study of the linear impulse response. *J. Fluid Mech.* **355**, 229–254.
- DONGARRA, J. J., STRAUGHAN, B. & WALKER, D. W. 1996 Chebyshev tau-QZ algorithm methods for calculating spectra of hydrodynamic stability problems. *Appl. Numer. Maths* **22** (4), 399–434.
- DRAZIN, P. G. & REID, W. H. 2004 *Hydrodynamic Stability*. Cambridge Mathematical Library 1. Cambridge University Press.
- EMERSON, B., LIEUWEN, T. & JUNIPER, M. P. 2016 Local stability analysis and eigenvalue sensitivity of reacting bluff-body wakes. *J. Fluid Mech.* **788**, 549–575.
- FRANCOIS, M. M., CUMMINS, S. J., DENDY, E. D., KOTHE, D. B., SICILIAN, J. M. & WILLIAMS, M. W. 2006 A balanced-force algorithm for continuous and sharp interfacial surface tension models within a volume tracking framework. *J. Comput. Phys.* **213** (1), 141–173.
- GORDILLO, J. M. & PÉREZ-SABORID, M. 2005 Aerodynamic effects in the break-up of liquid jets: on the first wind-induced break-up regime. *J. Fluid Mech.* **541**, 1–20.
- HAGERTY, W. & SHEA, J. F. 1955 A study of the stability of moving liquid film. *ASME J. Appl. Mech.* **22**, 509–514.
- HARVIE, D. J. E., DAVIDSON, M. R. & RUDMAN, M. 2006 An analysis of parasitic current generation in volume of fluid simulations. *Appl. Math. Model.* **30** (10), 1056–1066.
- HERBERT, T. 1997 Parabolized stability equations. *Annu. Rev. Fluid Mech.* **29** (1), 245–283.
- HIRT, C. W. & NICHOLS, B. D. 1981 Volume of fluid (VOF) method for the dynamics of free boundaries. *J. Comput. Phys.* **39** (1), 201–225.
- VAN HOOFT, J. A., POPINET, S., VAN HEERWAARDEN, C. C., VAN DER LINDEN, S. J. A., DE ROODE, S. R. & VAN DE WIEL, B. J. H. 2018 Towards adaptive grids for atmospheric boundary-layer simulations. *Boundary-Layer Meteorol.* **167** (3), 421–443.
- JARRAHBASHI, D. & SIRIGNANO, W. A. 2014 Vorticity dynamics for transient high-pressure liquid injection. *Phys. Fluids* **26** (10), 101304.

- KRÜGER, O., BOBUSCH, B. C., WOSZIDLO, R. & PASCHEREIT, C. O. 2013 Numerical modeling and validation of the flow in a fluidic oscillator. In *21st AIAA Computational Fluid Dynamics Conference, AIAA Paper 2013-3087*.
- LI, X. 1993 Spatial instability of plane liquid sheets. *Chem. Engng Sci.* **48** (16), 2973–2981.
- LI, X. & TANKIN, R. S. 1991 On the temporal instability of a two-dimensional viscous liquid sheet. *J. Fluid Mech.* **226**, 425–443.
- LIN, S. P., LIAN, Z. W. & CREIGHTON, B. J. 1990 Absolute and convective instability of a liquid sheet. *J. Fluid Mech.* **220**, 673–689.
- MANTIĆ-LUGO, V., ARRATIA, C. & GALLAIRE, F. 2014 Self-consistent mean flow description of the nonlinear saturation of the vortex shedding in the cylinder wake. *Phys. Rev. Lett.* **113** (8), 084501.
- MARMOTTANT, P. & VILLERMAUX, E. 2004 On spray formation. *J. Fluid Mech.* **498**, 73–111.
- MEHRING, C. & SIRIGNANO, W. A. 1999 Nonlinear capillary wave distortion and disintegration of thin planar liquid sheets. *J. Fluid Mech.* **388**, 69–113.
- NOACK, B. R., AFANASIEV, K., MORZYŃSKI, M., TADMOR, G. & THIELE, F. 2003 A hierarchy of low-dimensional models for the transient and post-transient cylinder wake. *J. Fluid Mech.* **497**, 335–363.
- OBERLEITHNER, K., PASCHEREIT, C. O. & WYGNANSKI, I. 2014a On the impact of swirl on the growth of coherent structures. *J. Fluid Mech.* **741**, 156–199.
- OBERLEITHNER, K., RUKES, L. & SORIA, J. 2014b Mean flow stability analysis of oscillating jet experiments. *J. Fluid Mech.* **757**, 1–32.
- ORSZAG, S. A. & CROW, S. C. 1970 Instability of a vortex sheet leaving a semi-infinite plate. *Stud. Appl. Maths* **49** (2), 167–181.
- OTTO, T. 2012 Spatio-temporal stability analysis in two-phase mixing layers. PhD thesis, Technische Universität Ilmenau.
- PIER, B. 2002 On the frequency selection of finite-amplitude vortex shedding in the cylinder wake. *J. Fluid Mech.* **458**, 407–417.
- POPINET, S. 2003 Gerris: a tree-based adaptive solver for the incompressible Euler equations in complex geometries. *J. Comput. Phys.* **190** (2), 572–600.
- POPINET, S. 2009 An accurate adaptive solver for surface-tension-driven interfacial flows. *J. Comput. Phys.* **228** (16), 5838–5866.
- RAYLEIGH, LORD 1878 On the instability of jets. *Proc. Lond. Math. Soc.* **s1-10** (1), 4–13.
- REYNOLDS, W. C. & HUSSAIN, A. K. M. F. 1972 The mechanics of an organized wave in turbulent shear flow. Part 3. Theoretical models and comparisons with experiments. *J. Fluid Mech.* **54** (2), 263–288.
- SCARDOVELLI, R. & ZALESKI, S. 1999 Direct numerical simulation of free-surface and interfacial flow. *Annu. Rev. Fluid Mech.* **31** (1), 567–603.
- SCHLICHTING, H. & GERSTEN, K. 2006 *Grenzschicht-theorie*. Springer.
- SCHMIDT, S., KRÜGER, O., GÖCKELER, K. & PASCHEREIT, C. O. 2018 Numerical investigation of the breakup behavior of an oscillating two-phase jet. *Phys. Fluids* **30** (7), 072101.
- SIPP, D. & LEBEDEV, A. 2007 Global stability of base and mean flows: a general approach and its applications to cylinder and open cavity flows. *J. Fluid Mech.* **593**, 333–358.
- SÖDERBERG, L. D. 2003 Absolute and convective instability of a relaxational plane liquid jet. *J. Fluid Mech.* **493**, 89–119.
- SQUIRE, H. B. 1953 Investigation of the instability of a moving liquid film. *British J. Appl. Phys.* **4** (6), 167–169.
- TAMMISOLA, O., LUNDELL, F. & SÖDERBERG, L. D. 2012 Surface tension-induced global instability of planar jets and wakes. *J. Fluid Mech.* **713**, 632–658.
- TAMMISOLA, O., SASAKI, A., LUNDELL, F., MATSUBARA, M. & SÖDERBERG, L. D. 2011 Stabilizing effect of surrounding gas flow on a plane liquid sheet. *J. Fluid Mech.* **672**, 5–32.
- TERHAAR, S., OBERLEITHNER, K. & PASCHEREIT, C. O. 2015 Key parameters governing the precessing vortex core in reacting flows: an experimental and analytical study. *Proc. Combust. Inst.* **35** (3), 3347–3354.

- TORREY, M. D., CLOUTMAN, L. D., MJOLSNESS, R. C. & HIRT, C. W. 1985 NASA-VOF2D: A computer program for incompressible flows with free surfaces. *Tech. Rep.* Los Alamos National Lab.
- TRYGGVASON, G., SCARDOVELLI, R. & ZALESKI, S. 2011 *Direct Numerical Simulations of Gas-Liquid Multiphase Flows*. Cambridge University Press.
- TURTON, S. E., TUCKERMAN, L. S. & BARKLEY, D. 2015 Prediction of frequencies in thermosolutal convection from mean flows. *Phys. Rev. E* **91** (4), 043009.
- YECKO, P. & ZALESKI, S. 2005 Transient growth in two-phase mixing layers. *J. Fluid Mech.* **528**, 43–52.
- YIH, C. 1967 Instability due to viscosity stratification. *J. Fluid Mech.* **27** (2), 337–352.
- ZANDIAN, A., SIRIGNANO, W. A. & HUSSAIN, F. 2018 Understanding liquid-jet atomization cascades via vortex dynamics. *J. Fluid Mech.* **843**, 293–354.